

## HERACLES: THE HERA CO LINE EXTRAGALACTIC SURVEY

ADAM K. LEROY<sup>1</sup>, FABIAN WALTER<sup>1</sup>, FRANK BIGIEL<sup>1</sup>, ANTONIO USERO<sup>2,3</sup>, AXEL WEISS<sup>4</sup>, ELIAS BRINKS<sup>2</sup>, W. J. G. DE BLOK<sup>5,6</sup>, ROBERT C. KENNICUTT<sup>7</sup>, KARL-FRIEDRICH SCHUSTER<sup>8</sup>, CARSTEN KRAMER<sup>9</sup>, H. W. WIESEMAYER<sup>8,9</sup>, AND HÉLÈNE ROUSSEL<sup>1,10</sup>

<sup>1</sup> Max-Planck-Institut für Astronomie, Königstuhl 17, D-69117, Heidelberg, Germany

<sup>2</sup> Centre for Astrophysics Research, University of Hertfordshire, Hatfield AL10 9AB, UK

<sup>3</sup> Observatorio Astronómico Nacional, C/ Alfonso XII, 3, 28014, Madrid, Spain

<sup>4</sup> MPIfR, Auf dem Hügel 69, 53121, Bonn, Germany

<sup>5</sup> Research School of Astronomy & Astrophysics, Mount Stromlo Observatory, Cotter Road, Weston ACT 2611, Australia

<sup>6</sup> Department of Astronomy, University of Cape Town, Private Bag X3, Rondebosch 7701, South Africa

<sup>7</sup> University of Cambridge, Institute of Astronomy, Madingley Road, Cambridge CB3 0HA, UK

<sup>8</sup> IRAM, 300 rue de la Piscine, 38406 St. Martin d'Hères, France

<sup>9</sup> IRAM, Avenida Divina Pastora 7, E-18012 Granada, Spain

<sup>10</sup> Institut d'Astrophysique de Paris, CNRS et Université P. & M. Curie, 98 bis Blvd Arago, 75014 Paris, France

Received 2008 September 14; accepted 2009 March 16; published 2009 April 23

### ABSTRACT

We present the Heterodyne Receiver Array CO Line Extragalactic Survey, an atlas of CO emission from 18 nearby galaxies that are also part of The HI Nearby Galaxy Survey and the *Spitzer* Infrared Nearby Galaxies Survey. We used the HERA multipixel receiver on the IRAM 30-m telescope to map the CO  $J = 2 \rightarrow 1$  line over the full optical disk (defined by the isophotal radius  $r_{25}$ ) of each target, at  $13''$  angular resolution and  $2.6 \text{ km s}^{-1}$  velocity resolution. Here we describe the observations and reduction of the data and show channel maps, azimuthally averaged profiles, integrated intensity maps, and peak intensity maps. The implied  $\text{H}_2$  masses range from  $7 \times 10^6$  to  $6 \times 10^9 M_\odot$ , with four low metallicity dwarf irregular galaxies yielding only upper limits. In the cases where CO is detected, the integrated  $\text{H}_2$ -to-HI ratios range from 0.02 to 1.13 and  $\text{H}_2$ -to-stellar mass ratios from 0.01 to 0.25. Exponential scale lengths of the CO emission for our targets are in the range 0.8–3.2 kpc, or  $0.2 \pm 0.05 r_{25}$ . The intensity-weighted mean velocity of CO matches that of HI very well, with a  $1\sigma$  scatter of only  $6 \text{ km s}^{-1}$ . The CO  $J = 2 \rightarrow 1/J = 1 \rightarrow 0$  line ratio varies over a range similar to that found in the Milky Way and other nearby galaxies,  $\sim 0.6$ – $1.0$ , with higher values found in the centers of galaxies. The typical line ratio,  $\sim 0.8$ , could be produced by optically thick gas with an excitation temperature of  $\sim 10 \text{ K}$ .

*Key words:* galaxies: ISM – ISM: molecules – radio lines: galaxies

### 1. INTRODUCTION

Molecular hydrogen,  $\text{H}_2$ , is the phase of the interstellar medium (ISM) most closely related to star formation. Clouds of molecular gas are thought to be birthplaces of virtually all stars, and  $\text{H}_2$  often dominates the mass budget of the ISM in the inner, most vigorously star-forming parts of spiral galaxies ( $\lesssim 0.5 r_{25}$ ). Unfortunately,  $\text{H}_2$  lacks a dipole moment, and typical temperatures in giant molecular clouds (GMCs) are too low to excite quadrupole or vibrational transitions. Therefore, indirect approaches are required to estimate the distribution of molecular hydrogen. Although not without associated uncertainties, CO line emission remains the most straightforward and reliable tracer of  $\text{H}_2$  in galaxies. It is relatively bright and its ability to trace the bulk distribution of  $\text{H}_2$  has been confirmed via comparisons with gamma rays (e.g., Lebrun et al. 1983; Strong et al. 1988) and dust emission (e.g., Désert et al. 1988; Dame et al. 2001).

Since the first detections of CO emission from Milky Way molecular clouds (Wilson et al. 1970) and other galaxies (Rickard et al. 1975; Solomon & de Zafra 1975), a number of surveys have used CO to characterize the molecular content of galaxies. Young & Scoville (1991) summarize the first two decades of such observations, during which CO was observed in  $\sim 100$  galaxies. These data yielded a basic understanding of the radial distribution of CO in disk galaxies and the relationship between HI (atomic hydrogen),  $\text{H}_2$ , and star formation as a function of morphology. This number expanded to  $\sim 300$  with the publication of The Five

Colleges Radio Astronomy Observatory (FCRAO) Extragalactic CO Survey (henceforth the “FCRAO survey,” Young et al. 1995), which remains the definitive survey of CO in the local volume.

The FCRAO survey and most of its predecessors focused on the CO  $J = 1 \rightarrow 0$  transition, i.e., the transition between the first rotationally excited state and the ground state. Braine et al. (1993) observed both CO  $J = 2 \rightarrow 1$  and  $J = 1 \rightarrow 0$  emission from the centers of 81 galaxies (finding a typical line ratio of  $0.89 \pm 0.06$ ). These data support the idea that CO  $J = 2 \rightarrow 1$  emission is a viable tracer of  $\text{H}_2$  in other galaxies; Israel et al. (1984) and Sakamoto et al. (1995) showed that the distribution of CO  $J = 2 \rightarrow 1$  follows that of CO  $J = 1 \rightarrow 0$  in the Milky Way.

In the past decade, technical improvements—especially the construction of several millimeter-wave interferometers—have allowed higher resolution imaging of CO in galaxies. These have obtained maps of Local Group galaxies with spatial resolution matched to the sizes of individual GMCs (e.g., Fukui et al. 1999; Engargiola et al. 2003; Leroy et al. 2006; Rosolowsky 2007) and observations of large samples of more distant galaxies with resolutions of only a few hundred parsecs (e.g., Walter et al. 2001; Sakamoto et al. 1999). Of particular note, the Berkeley Illinois Maryland Association Survey of Nearby Galaxies (BIMA SONG; Helfer et al. 2003) mapped CO emission at  $\sim 6''$  resolution in 44 nearby spirals. The relatively wide extent of the BIMA SONG maps (typical full width  $\sim 190''$ ) makes this survey the first to systematically map the disks of normal spiral galaxies with resolution matched to the scales over

which GMCs, the basic units of the molecular ISM, are believed to form.

Over the past few years another technical improvement, heterodyne receiver arrays on single-dish telescopes observing at 1–3 mm, has made it possible to efficiently map CO emission from large areas of the sky. This allows complete inventories of molecular gas in samples of nearby galaxies that were prohibitive with single-pixel receivers (the FCRAO survey, by contrast, only sampled the major axes of its targets). Schuster et al. (2007) demonstrated this capability by using the Heterodyne Receiver Array (HERA, Schuster et al. 2004) on the IRAM 30-m telescope to map CO  $J = 2 \rightarrow 1$  emission from the whole disk of M 51. Kuno et al. (2007) presented CO  $J = 1 \rightarrow 0$  maps of 40 nearby spirals, largely carried out using the BEARS focal plane array on the Nobeyama 45 m. In both cases, the large diameter of the telescopes (and the fact that HERA observes at 230 GHz) ensure a resolution of 11–15", adequate to resolve spiral structure, bars, rings, and large star-forming complexes.

Here we present the HERA CO Line Extragalactic Survey (HERACLES). HERACLES is a new survey of CO emission in nearby galaxies carried out with the HERA receiver array on the IRAM 30-m telescope.<sup>11</sup> The main motivation for this new survey is to quantify the relationship between atomic gas, molecular gas, and star formation in a significant sample of galaxies. To meet this goal, HERACLES differs from previous CO surveys in two main ways: the area surveyed and the sample.

In contrast to the FCRAO survey or BIMA SONG, we map the whole optical disk of each galaxy with full spatial sampling and good sensitivity. Despite the large area surveyed, we still achieve a relatively good resolution of 13",  $\sim 500$  pc at the median distance of our sample. Because we use a single dish telescope rather than an interferometer, we are sensitive to extended structure that may be missed by the latter (which do not recover extended structure on the sky by design).

The HERACLES sample overlaps that of The H I Nearby Galaxy Survey (Walter et al. 2008) and the *Spitzer* Infrared Nearby Galaxies Survey (Kennicutt et al. 2003), ensuring an immediately accessible multiwavelength database spanning from radio to UV. These data offer windows on the diffuse ISM, dust, embedded star formation, photodissociation regions, and both young and old stars.

This paper describes the HERACLES observing (Section 2) and data reduction (Section 3) strategies. We show the distribution of CO emission (Section 4) and compare HERACLES results to previous observations of the H I 21 cm (Section 5.3) and the CO  $J = 1 \rightarrow 0$  (Section 5.4) lines in the same galaxies. Two papers present the first round of in-depth scientific analysis. In Bigiel et al. (2008), we combine HERACLES with H I, IR, and UV data to measure the relationship between the surface densities of H I, H<sub>2</sub>, and star formation rate (the ‘‘Schmidt Law’’). In Leroy et al. (2008), we use the same data to measure the star formation per unit gas as a function of environment, comparing these measurements to proposed theories.

## 2. OBSERVATIONS

The HERACLES sample consists of galaxies that are targets of THINGS, far enough north to be easily observed by the 30-m, and not prohibitively large ( $\lesssim 12 \times 12'$ ). These 18 spiral and irregular galaxies are listed in Table 1. We draw the inclination,

**Table 1**  
HERACLES Sample

Galaxy	Dist. (Mpc)	Incl. ( $^\circ$ )	P.A. <sup>a</sup> ( $^\circ$ )	$r_{25}$ <sup>b</sup> ( $'$ )
NGC 628	7.3	7	20	4.9
NGC 925	9.2	66	287	5.3
Holmberg II	3.4	41	177	3.8
NGC 2841	14.1	74	154	5.3
NGC 2903	8.9	65	204	5.9
Holmberg I	3.8	12	50	1.6
NGC 2976	3.6	65	335	3.6
NGC 3184	11.1	16	179	3.7
NGC 3198	13.8	72	215	3.2
IC 2574	4.0	53	56	6.4
NGC 3351	10.1	41	192	3.6
NGC 3521	10.7	73	340	4.2
NGC 4214	2.9	44	65	3.4
NGC 4736	4.7	41	296	3.9
DDO 154	4.3	66	230	1.0
NGC 5055	10.1	59	102	5.9
NGC 6946	5.9	33	243	5.7
NGC 7331	14.7	76	168	4.6

**Notes.**

<sup>a</sup> Position angle of major axis, measured north through east.

<sup>b</sup> Radius of the  $B$ -band 25 mag arcsec<sup>-2</sup> isophote.

position angle, and distances in this table from Walter et al. (2008) and the isophotal radius,  $r_{25}$ , from the LEDA database.

From January 2006 through March 2008, we used the HERA on the IRAM 30-m telescope to map CO  $J = 2 \rightarrow 1$  emission from these galaxies. HERA is a multipixel receiver that simultaneously observes 9 positions on the sky at two orthogonal linear polarizations.

We tuned HERA to observe the CO  $J = 2 \rightarrow 1$  transition near 230 GHz and attached the HERA receivers to the Wideband Line Multiple Autocorrelator (WILMA) backend. WILMA consists of 18 units, each with 2 MHz channel width and 930 MHz bandwidth, yielding a velocity resolution of 2.6 km s<sup>-1</sup> and velocity coverage of 1200 km s<sup>-1</sup> at the wavelength of the CO  $J = 2 \rightarrow 1$  line.

Table 2 (Column 4) gives the dates when individual galaxies were observed. We generally observed only under good winter conditions, meaning zenith opacities  $\tau < 0.3$  at 225 GHz. During most runs, the opacity was better than this, often  $\lesssim 0.1$ . System temperatures varied with pixel, receiver, and semester but typical values were 275–350 K for the 9 receiver pixels of the first polarization (HERA1) and 350–450 K for the 9 receiver pixels of the second polarization (HERA2). On average, data from one pixel (not always the same one) could not be used due to unreliable baselines. During a few days, indicated in Table 2, only one polarization was usable.

We used on-the-fly mapping mode and scanned across the galaxy at 8" s<sup>-1</sup>, writing out a spectrum every 0.5 s, i.e., integrating over 4" of scanning. Approximately every 2 minutes, we observed a reference position near the galaxy for 10–15 s. This was chosen using the THINGS H I maps to pick a position free of gas that lies outside but near the optical disk of the galaxy. Every 10–15 minutes we calibrated the intensity scale of the data using sky emission from the reference position and the backend counts from loads at ambient and cold (liquid nitrogen) temperatures.

In most cases, the target area was the optical disk of the galaxy, defined by the 25th magnitude  $B$ -band isophote ( $r_{25}$ ), though in

<sup>11</sup> IRAM is supported by CNRS/INSU (France), the MPG (Germany) and the IGN (Spain).

**Table 2**  
Observing Dates and Orientation

Galaxy	Scan P.A. <sup>a</sup> (°)	Scan Legs <sup>b</sup>	Dates Observed	Spectra <sup>c</sup> (10 <sup>4</sup> )
NGC 628	0	9 × 9	2007 Jan 10, 12, 13, 14	105
NGC 925	287	9 × 4	2007 Oct 23 <sup>d</sup> , 30; 12 <sup>e</sup> ; 2008 Jan 13; 2008 Mar 25, 26	55
Holmberg II	0	5 × 5	2008 Feb 21, 22	28
NGC 2841	153	6 × 2	2007 Oct 26, 27, 30	31
NGC 2903	204	10 × 4	2007 Nov 27 <sup>d</sup> ; 2008 <sup>e</sup> Feb 13, 16, 17, 21	87
Holmberg I	0	3 × 3	2007 Oct 30; 2007 Nov 1, 3	18
NGC 2976	335	6 × 3	2007 Oct 27, 28, 31; 2007 Nov 3	44
NGC 3184	0	6 × 6	2007 Oct 31; 2007 Nov 1, 4, 5	66
NGC 3198	215	6 × 2	2007 Oct 26, 28; 2007 Nov 2	31
IC 2574	55	11 × 6	2008 Feb 17, 21, 22, 25, 27; 2008 Mar 25, 26	125
NGC 3351	0	6 × 6	2007 Oct 31; 2007 Nov 1, 2; 2008 Jan 17	70
NGC 3521	340	7 × 3	2007 Nov 2, 3, 4	50
NGC 4214	65	4 × 4	2007 Nov 5; 2008 Jan 10, 11, 12	38
NGC 4736	0	8 × 4	2007 Jan 19, 20; 2007 Feb 21, 24 <sup>d</sup> , 25, 26	75
DDO 154	230	4 × 2	2008 Feb 13, 16	16
NGC 5055	0	13 × 5	2007 Jan 13 <sup>e</sup> , 14, 15, 16	95
NGC 6946	0	11 × 11	2007 Jan 13, 14, 15, 17, 18, 19	207
NGC 7331	168	8 × 3	2007 Oct 23 <sup>d</sup> , 24 <sup>d</sup> , 26, 27; 2008 Jan 10, 11, 12	63

**Notes.**

<sup>a</sup> Orientation of major axis scans measured from north through east. See Figure 1.

<sup>b</sup> Number of fully sampled (i.e., back and forth) scans along short × long edge. Width of one scan is  $\sim 68''$ .

<sup>c</sup> Number of spectra in the final reduction. Each represents an 0.5 s integration by one polarization on one receiver. One hour integrating on source yields  $\approx 13 \times 10^4$  spectra.

<sup>d</sup> For this day, we adjusted the rejection threshold to remove more than the 10% of spectra with the highest rms about the baseline fit (see Section 3.3).

<sup>e</sup> For this day, only one polarization was usable.

several galaxies we extended the map to probe obvious H I peaks or filaments outside the optical disk.

To construct a single map of a galaxy, we observed the target area using a series of parallel scans. These “long-edge” scans were usually aligned with the major axis of the galaxy and were spaced to cover the whole target area. We then immediately made a series of “short-edge” scans covering the same area, but oriented perpendicular to the original long-edge scans. The goal of this cross-hatched observing strategy was to minimize artifacts in the final data by ensuring that each area of the sky was observed by many different receivers. Figure 1 illustrates this approach for NGC 3521, an inclined Sb galaxy. The beam-print of the array is shown at the reference position and arrows over the body of the galaxy indicate individual scans. Here there are three “long-edge” scans and seven “short-edge” scans. The second and third columns in Table 2 give the orientation of the long edge—measured north through east—and the number of scans along the short and long edges ( $7 \times 3$  for NGC 3521).

In order to fully sample the  $11''$  (FWHM) beam of the 30 m, we used the derotator to rotate the beam pattern of HERA by  $9:5$  relative to the direction of scanning.<sup>12</sup> This yields a pixel spacing of  $\approx 4''$  on the sky but leaves a gap between the HERA pixels, which are separated by  $28''$ . We filled this gap by offsetting the next scan by  $11:9$  perpendicular to the scan direction and then repeating the original scan leg in reverse. This strategy yields a fully sampled map with spectra spaced by  $4''$  both along and perpendicular to the scan direction.

We repeated the full set of long and short-edge scans 15–20 times for each galaxy. This yielded the equivalent of 2–3 minutes

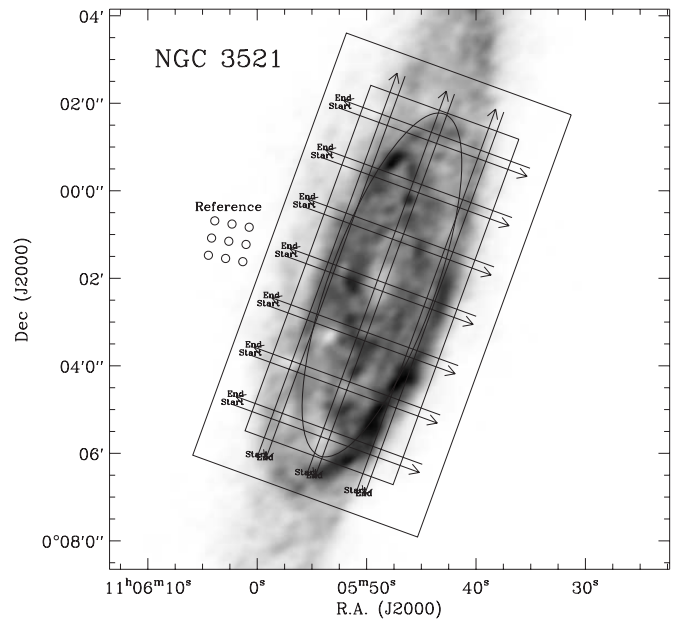


**Figure 1.** Our observing strategy illustrated for the inclined spiral galaxy NGC 3521. The gray-scale image shows the THINGS H I column density map (Walter et al. 2008) and the oval indicates  $r_{25}$ , our target area. Arrows indicate the length and direction of individual scan legs, which form back-and-forth pairs that together yield a fully sampled map. To cover the galaxy, we use seven back-and-forth scans along the short edge and three along the long edge (indicated by the entry  $7 \times 3$  in Column 3 of Table 2). The beam print of HERA appears at the reference position, which was chosen to be free of gas but near the galaxy. Concentric rectangles show the areas of full (inner) and partial (outer) sensitivity.

<sup>12</sup> For a full description and illustration of this observing mode, see the HERA User Manual (Version 2) by Schuster et al. (2007), available online at <http://www.iram.fr/IRAMES>.

of integration per independent beam. The fifth column in Table 2 lists the number of individual spectra used in the final data cube

for each galaxy (in units of  $10^4$ ). Each spectra corresponds to a 0.5 s integration with one receiver, so that the full 18-element array produces 36 spectra each second of on-source integration and an hour on source produces  $13 \times 10^4$  spectra. Note that these numbers come after rejection of high-rms spectra and removal of bad pixels (Section 3) and that this time estimate takes no account of reference observations, calibrations, slewing, tuning, or other overheads.

### 3. REDUCTION

#### 3.1. Basic Calibration and Reference Subtraction

We carried out the basic data reduction using the Multi-channel Imaging and Calibration Software for Receiver Arrays (MIRA),<sup>13</sup> which is part of the Grenoble Image and Line Data Analysis Software (GILDAS) package.<sup>14</sup> This consisted of combining each scan with the nearest reference measurement and calibration observation via

$$T_A^* = T_{\text{cal}} \times \frac{On - Off}{Hot - Off}. \quad (1)$$

Here *On* refers to the backend count rate from the on-source measurement, *Off* to the count rate from the reference (empty sky) measurements before and after the on-source measurement, *Hot* to the count rate from the ambient load during the calibration observation, and  $T_{\text{cal}}$  to a calibration factor determined from the calibration observation.<sup>15</sup> The resulting antenna temperature,  $T_A^*$ , is defined to be the brightness temperature of a source filling the entire  $2\pi$  steradians in front of the telescope and outside the atmosphere.

The data, in units of  $T_A^*$ , were written out for further reduction using the Continuum and Line Analysis Single-dish Software (CLASS) package, which is also part of GILDAS.

#### 3.2. Fitting Baselines Based on H I Velocity

After this basic reduction, total power variations in both the receiver and the atmosphere and nonlinearities in the backend and receiver still made it necessary to fit baselines to individual spectra before combining them into data cubes. Because the data total  $> 10^7$  spectra, this needed to be done in an automated manner.

The CO line typically covers a small but variable part of the bandpass, so fitting a linear baseline to a single wide window did not yield satisfactory results. Instead, we used the THINGS H I data cubes to define the region of the spectrum likely to contain the CO line and to fit a linear baseline to a restricted part of the spectrum. This yielded good results and was straightforward to automate. The underlying assumption is that H I and H<sub>2</sub> (traced by CO) are reasonably well mixed, so that the mean velocity of CO emission is similar to the mean H I velocity. This is a reasonable expectation: the two lines both trace dissipative gas moving in the same potential well and H<sub>2</sub> is believed to form out of H I. In Section 5.3 we use our data to verify this assumption, indeed finding an excellent match between the mean velocities of H I and CO.

The exact approach, illustrated in Figure 2, was:

1. We defined a window over which the CO line was likely to appear. This window was centered on the mean H I velocity and 60–300 km s<sup>-1</sup> wide, depending on the galaxy. For many galaxies, we defined two windows: one used near the center of the galaxy and another used over the rest of the disk with the fitting region varying smoothly between the two regimes. We selected the window widths for each galaxy based on a preliminary reduction.
2. Adjacent to this window, we defined two regions of the spectrum that we used to fit a linear baseline. These had the same width as the central window, which was not included in the fit. The fit is subtracted from the whole spectrum.
3. We blank all data outside the fitting windows, so that only the fitting windows and the central region—the likely location of signal—are left.

In this way, we fit baselines to all spectra in each galaxy. We reduced each data cube three times. First, we made a crude reduction fitting baselines to a fairly wide area around the H I line. Based on the results, we refined the fitting region (white areas in Figure 2, step 1 above), defining a central window that was as narrow as possible while still including all of the CO emission seen in the preliminary reduction. With the third reduction, we iterated the process, using the second reduction to further refine our fitting regions and more carefully identifying and removing pathological data (Section 3.3).

#### 3.3. Rejecting Remaining Pathological Spectra

A small fraction of spectra are still not well fit by our approach. If included in the final data cube, these introduce artifacts and obscure signal. To remove them in a straightforward, systematic way, we discard the 10% of the data with the highest rms residuals about the baseline fit from each day of observing (note that these residuals are determined from the fitting region, which is chosen to be signal free). Removing 10% of the data causes a negligible decrease in signal to noise but removing the pathological spectra yields a noticeable increase in the quality of the data cubes. In a few cases where a clear population of high rms spectra survive the baseline fitting, we adjust the rejection threshold to reject more data (these observations are indicated in Table 2). Typical values for the 90th percentile are rms ( $T_A^*$ )  $\sim 0.35$ – $0.7$  K for 2.6 km s<sup>-1</sup> wide channels.

#### 3.4. Constructing a Data Cube

We combine the reduced spectra into a table and use the CLASS gridding routine `xy_map` to construct a data cube with 2'' pixel size and 2.6 km s<sup>-1</sup> channel width. This routine convolves the irregularly gridded OTF data with a Gaussian kernel with a full width of  $\sim 1/3$  the FWHM beam size, yielding a final angular resolution approximately 11'' and noise correlated on scales of 4''.

Because the noise is correlated on scales that are small compared to the beam (response to astronomical signal), smoothing the data slightly offers a significant gain in sensitivity while minimally degrading the beam size (e.g., Mangum et al. 2007). In the rest of this paper, we show data that have been convolved with a 7'' (FWHM) Gaussian, yielding a final resolution of 13''.

We converted the units of the data cube from antenna temperature,  $T_A^*$ , to main beam temperature,  $T_{\text{MB}}$ . Main beam temperature is the temperature of a source filling only the main beam of the telescope (recall that  $T_A^*$  refers to a source

<sup>13</sup> <http://www.iram.fr/IRAMFR/GILDAS/doc/html/mira-html/mira.html>

<sup>14</sup> <http://www.iram.fr/IRAMFR/GILDAS>

<sup>15</sup> For a full discussion of the “chopper wheel” calibration applied to the IRAM

30-m telescope, see “Calibration of Spectral Line Data at the IRAM 30 m Telescope” by Kramer (1997) available online at <http://www.iram.fr/IRAMES>.

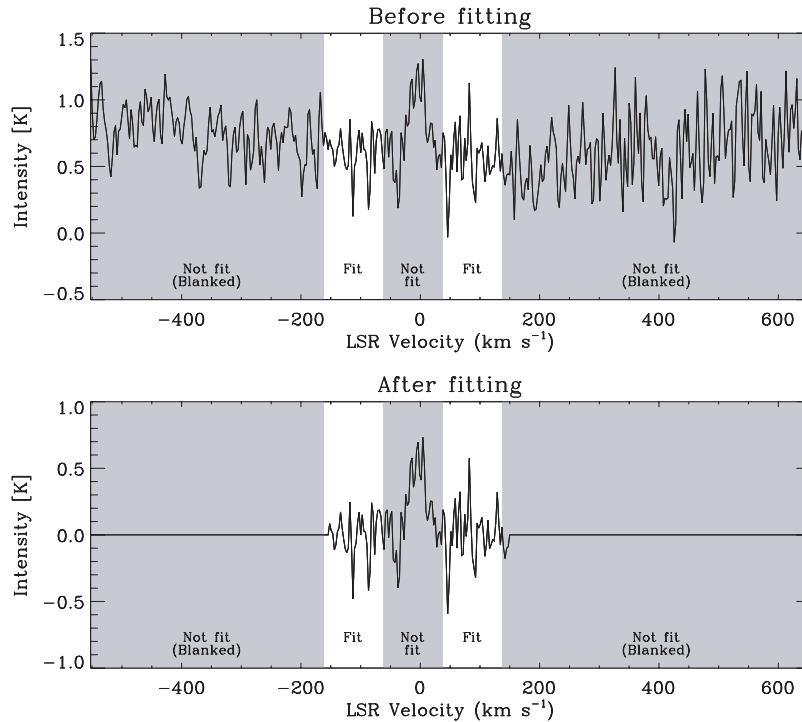


**Figure 2.** Our approach to baseline fitting, illustrated for a single (0.5 s) spectrum of NGC 6946. We use the mean H I velocity to predict the likely velocity of CO emission. From this, we define three regions: one near the line that is likely to contain signal and two that are close to the line but displaced enough not to contain signal. We use the data in these two adjacent regions to fit a first-order baseline (while avoiding the central region). We subtract this baseline from the whole spectrum and discard data outside the fitting regions.

filling the full forward  $2\pi$  of the sky). To convert from  $T_A^*$  to  $T_{MB}$ , we replaced the forward efficiency,  $F_{\text{eff}} = 0.91$ , with the main beam efficiency,  $B_{\text{eff}} = 0.52$ , yielding  $T_{MB} = 0.91/0.52T_A^* = 1.75T_A^*$  (efficiencies were adopted from the 30-m online documentation). For the remainder of the paper, we work in units of  $T_{MB}$ .

### 3.5. Uncertainties

Table 3 lists the rms noise for each galaxy (Column 2). We estimate this from signal-free parts of the cube, which has  $13''$  angular resolution and  $2.6 \text{ km s}^{-1}$  channel width. Typical values are in the range 20–25 mK. Mostly this noise averages in the expected manner, but on very large scales our method of calibration introduces an additional consideration. Because we subtract the same reference measurements from all spectra along an individual scan leg (Section 2), low level correlated noise is present in the maps. As a result, the rms noise of spectra derived from integrating entire data cubes is 2–3 times higher than expected from averaging independent, normal noise; this ratio is consistent with the ratio of observing time spent on the reference to that on source.

We calculated how the integrated intensity of regions with very high ( $\gtrsim 50$ ) signal-to-noise ratio (SNR) varied when measured with different polarizations and on different days. We identified such regions in NGC 2903, 3351, 3521, 5055, and 6946 and then reduced the data separately for each day and polarization. The rms day-to-day scatter in the integrated intensity from these high SNR regions is  $\sim 20\%$ . This is an approximate, but by no means rigorous, measure of the uncertainty in the calibration of the telescope (e.g., it includes the effect of pointing errors but not the uncertainty in the assumed efficiencies of the telescope).

We tested the uncertainty associated with our method of reduction and baseline fitting by reducing all of the data for

one galaxy independently. We flagged bad data and identified baseline fitting regions by eye. Over regions of significant emission ( $I_{\text{CO}} > 2\sigma$  in 3 successive channels at  $30''$  resolution) the two reductions agree very well. The best-fit line relating our automated reduction to the “by-hand” one in these regions has a slope of 1.01 and an intercept of  $0.06 \text{ K km s}^{-1}$ . Along lines of sight with strong CO emission ( $I_{\text{CO}} > 2.6 \text{ K km s}^{-1}$ ), the ratio of the two reductions scatters by 10% (rms). This check offers an estimate of the uncertainty associated with how we carry out the data reduction and verifies that our automated approach (which is less subjective and much simpler to apply) agrees well with a “by-hand” reduction.

A final important uncertainty is related to our observing strategy. In some cases, pixel-to-pixel variations in gain, system temperature, and bandpass shape leave the imprint of our cross-hatch observing strategy in the data. This may be seen in the channel and integrated intensity maps present (Section 4) as striping along the two scan directions (i.e., it is possible to see the scanning path of individual pixels in the noise). The magnitude of this striping is usually comparable to or below that of the statistical noise and mostly these artifacts do not obscure or mimic signal. The exceptions are four highly inclined spirals—NGC 2841, 2903, 3521, and 7331—in which significant striping is visible in individual channel maps. The likely cause is a breakdown in our baseline fitting: because the CO line is often wide in these galaxies, we are forced to use relatively broad fitting windows.

## 4. THE DISTRIBUTION OF CO $J = 2 \rightarrow 1$ EMISSION

Our basic result is the distribution of CO  $J = 2 \rightarrow 1$  emission in our 18 targets. In 14 galaxies, extended emission is clearly detected. Here, we show that emission using channel maps, peak intensity maps, integrated intensity maps, and radial profiles.

**Table 3**  
Basic Results

Galaxy	$\sigma_{\text{rms}}$ (mK)	$F_{\text{CO}}$ ( $10^5 \text{ K km s}^{-1} \text{ arcsec}^2$ )	$L_{\text{CO}}$ ( $10^7 \text{ K km s}^{-1} \text{ pc}^2$ )	$l_{\text{CO}}$ (kpc)	$d_{\text{max}}$ ( $r_{25}$ )	$M_{\text{H}_2}/M_{\text{HI}}$	$M_{\text{H}_2}/M_*$	$(M_{\text{H}_2} + M_{\text{HI}})/M_*$
NGC 628	22	1.8	23	2.4	0.72	0.24	0.10	0.52
NGC 925	21	0.25	4.9	3.2	0.17	0.04	0.04	0.90
Holmberg II	36	<0.10 <sup>a</sup>	<0.33 <sup>a</sup>	...	...	...	...	>3.6
NGC 2841	44	0.61	28	...	0.65	0.13	0.03	0.22
NGC 2903	23	2.9	53	1.6	0.47	0.50	0.25	0.77
Holmberg I	24	<0.34 <sup>a</sup>	<0.94 <sup>a</sup>	...	...	...	...	>7.2
NGC 2976	21	0.40	1.2	1.2	0.53	0.36	0.05	0.18
NGC 3184	20	1.0	30	2.9	0.55	0.39	0.09	0.33
NGC 3198	17	0.25	11	2.7	0.43	0.04	0.04	1.03
IC 2574	33	<0.74 <sup>a</sup>	<2.8 <sup>a</sup>	...	...	...	...	>3.8
NGC 3351	20	0.78	19	2.5	0.41	0.63	0.05	0.12
NGC 3521	22	2.8	76	2.2	0.95	0.38	0.08	0.29
NGC 4214	18	0.09	0.17	...	0.33	0.02	0.01	0.80
NGC 4736	23	2.2	11	0.8	1.33	1.13	0.03	0.06
DDO 154	18	<0.05 <sup>a</sup>	<0.21 <sup>a</sup>	...	...	...	...	>34.8
NGC 5055	24	4.1	98	3.1	0.67	0.43	0.08	0.26
NGC 6946	25	10.8	88	1.9	0.86	0.86	0.16	0.35
NGC 7331	20	2.2	113	3.1	0.61	0.50	0.07	0.21

**Notes.** Column 1: galaxy; Column 2: rms intensity in a 2.6 km s<sup>-1</sup>-wide channel map with 13'' (FWHM) angular resolution; Column 3: integrated flux of CO emission (see Equation (2) for conversion to Jy km s<sup>-1</sup>); Column 4: integrated luminosity of CO emission (see Equation (3) for conversion to H<sub>2</sub> mass); Column 5: exponential scale length of CO emission; Column 6: radius of most extended high SNR detection (Section 4.2); Column 7: ratio of H<sub>2</sub> to H I mass; Column 8: ratio of H<sub>2</sub> to stellar mass; Column 9: ratio of total gas (H<sub>2</sub> + H I) to stellar mass.

<sup>a</sup> 5 $\sigma$  upper limits.

We make several basic measurements, summarized in Table 3, including the integrated flux, luminosity, and exponential scale length.

#### 4.1. Channel, Integrated, and Peak Intensity Maps

Figures 3–16 show channel maps (i.e., intensity integrated over a succession of velocity ranges) of each clearly detected galaxy. These span approximately the velocity range over which we find CO emission and show the area of uniform sensitivity (i.e., the inner rectangle in Figure 1). The gray scale and final channel width vary from galaxy to galaxy and are indicated in each caption. Data at velocities outside the baseline fitting region (Section 3.2) are blanked in the reduction and appear as zeroes (smooth gray regions) in the channel maps.

The left column in Figures 17–30 shows integrated intensity for the same 14 galaxies. A bar next to each figure indicates the color stretch, which varies from galaxy to galaxy. Contours in the integrated intensity maps run from 1 K km s<sup>-1</sup> (gray), increasing by factors of 2 each step. The first black contour,  $I_{\text{CO}} = 2 \text{ K km s}^{-1}$ , corresponds to  $\Sigma_{\text{H}_2} \sim 11 M_{\odot} \text{ pc}^{-2}$  in a face-on spiral galaxy (Equation (4)). This approximately indicates where the ISM is dominated by H<sub>2</sub>. The first white contour,  $I_{\text{CO}} = 32 \text{ K km s}^{-1}$ , corresponds to  $\sim 176 M_{\odot} \text{ pc}^{-2}$ , roughly the surface density of an individual Galactic GMC (Solomon et al. 1987). Regions with such high surface densities over a large area are rare but not unknown in our survey (e.g., the bar of NGC 2903 and the centers of NGC 2903, 3351, 4736, 5055, 6946).

We created the integrated intensity maps by summing along the velocity axis over regions that contain signal. To identify these regions, we first smooth the data to 30'' angular resolution and bin to reach a velocity resolution equal to half the width of the channel maps (this varies with galaxy, see Figures 3–16).

All regions with  $I_{\text{CO}} > 3\sigma$  in two consecutive velocity channels in these low resolution cubes were labeled “signal,” and we integrated the original cube over these regions to yield the maps in Figures 17–30. This procedure has a low false positive rate ( $\lesssim 1$  expected per cube) so that most emission seen here is real with high confidence, though in a few cases (NGC 2841, 2903, 7331) artifacts from baseline fitting persist. Because the condition to identify signal is fairly restrictive these maps are not ideal indicators of low brightness, extended emission.

The peak intensity maps in the right column of Figures 17–30 give a clearer view of the area mapped, extent of low brightness emission, and morphology. These are created by measuring the peak brightness along each line of sight at 2.6 km s<sup>-1</sup> velocity resolution. This procedure suppresses the worst artifacts in our data, which tend to persist at a low level over many consecutive channels. It also lowers the contrast between bright and faint regions, which arise partially from differences in the line width. As a result, several interesting low-lying features are visible in these maps: e.g., arms extending out from the molecular rings in NGC 3521 and NGC 7331; faint filamentary structure in the disk of NGC 4736; and a faint, previously unidentified molecular complex in the southwest of the dwarf starburst NGC 4214 (see Walter et al. 2001).

Peak intensity maps of inclined systems tend to show radial structure on small scales. In order for emission to add constructively in such a map, it must be at the same velocity. When a galaxy with a rapidly changing velocity field is observed with finite angular resolution and then collapsed to a peak intensity map, signal will tend to be smoothed along isovelocity contours, leaving them faintly visible in the final image.

The channel, integrated, and peak intensity maps show extended molecular structures covering the inner part of the disk in most of our galaxies. The detailed morphologies are fairly varied. Spiral structure is particularly evident in the Sc galaxies

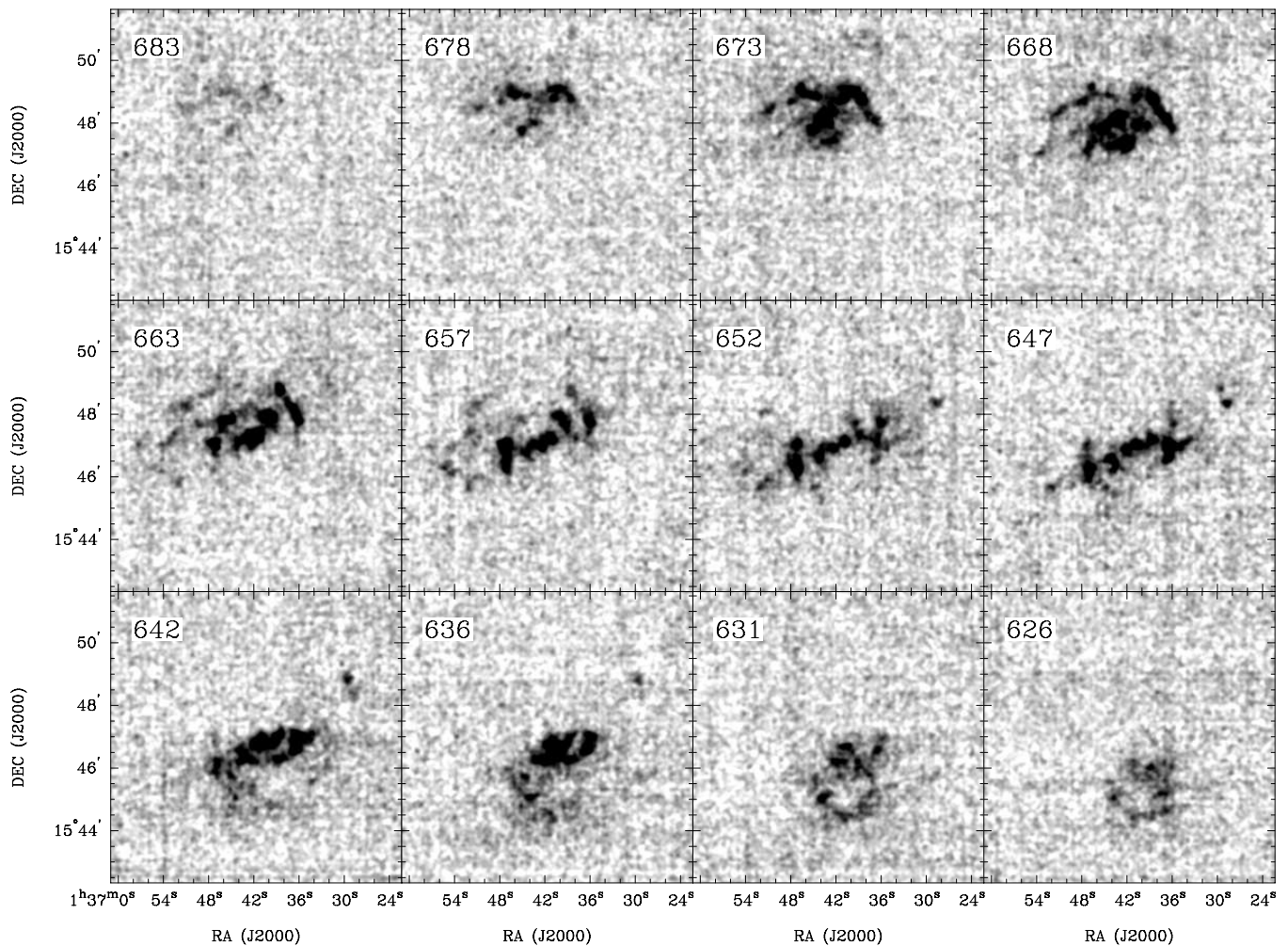


**Figure 3.** Channel maps for NGC 628 at  $13''$  resolution. The gray-scale runs from  $-0.025$  to  $0.15$  K. Each channel is  $5.2 \text{ km s}^{-1}$  wide and the rms intensity in one channel is  $19 \text{ mK}$ . The central LSR velocity for each channel (in  $\text{km s}^{-1}$ ) appears in the top left corner of the map.

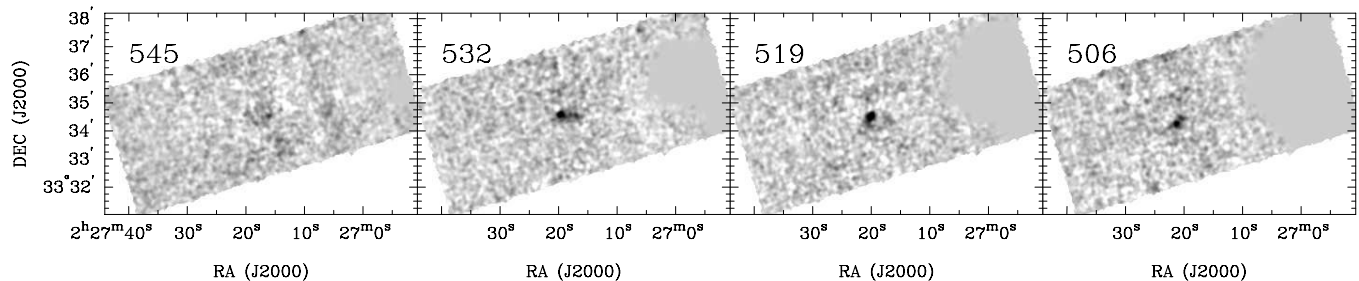


**Figure 4.** Channel maps for NGC 925 at  $13''$  resolution. The gray-scale runs from  $-0.025$  to  $0.10$  K. Each channel is  $13 \text{ km s}^{-1}$  wide and the rms intensity in one channel is  $12 \text{ mK}$ . The smooth gray area indicates data at velocities outside the baseline fitting window, which are blanked during the reduction (Section 3.2).

NGC 628, NGC 3184, and NGC 6946. NGC 2903 is dominated by a central, bright bar. The Sb galaxies NGC 3351 and NGC 7331 both show well-defined molecular rings and similar structures are suggested by the channel maps for NGC 2841 and NGC 3198. Molecular gas completely covers the inner parts of NGC 3521, NGC 4736, and NGC 5055. Over this area, NGC 3521 and NGC 4736 show ring-like structure and outside this central region, NGC 3521, NGC 4736, NGC 5055, and NGC 7331 show spiral structure. The late-type galaxies NGC 925 and NGC 4214 both show only faint CO emission, which is common for late-type galaxies. The other low mass galaxy that we detect, NGC 2976, defies this trend, showing bright CO dominated by two large star-forming complexes.

#### 4.2. Radial Profiles

Despite different morphologies, our targets show a common behavior on large scales: azimuthally averaged CO intensity declines steadily as a function of radius in most galaxies. This is clear from Figure 31, in which we plot integrated intensity as a function of radius for each detected galaxy. To make these profiles, we collapse the data cubes without masking into integrated intensity maps and then average these over a series of concentric tilted rings. These rings assume the position angle and inclinations in Table 1 and are each  $10''$  in width, about 1 resolution element. Note that these profiles do not include any correction for inclination (i.e., they correspond to the observed

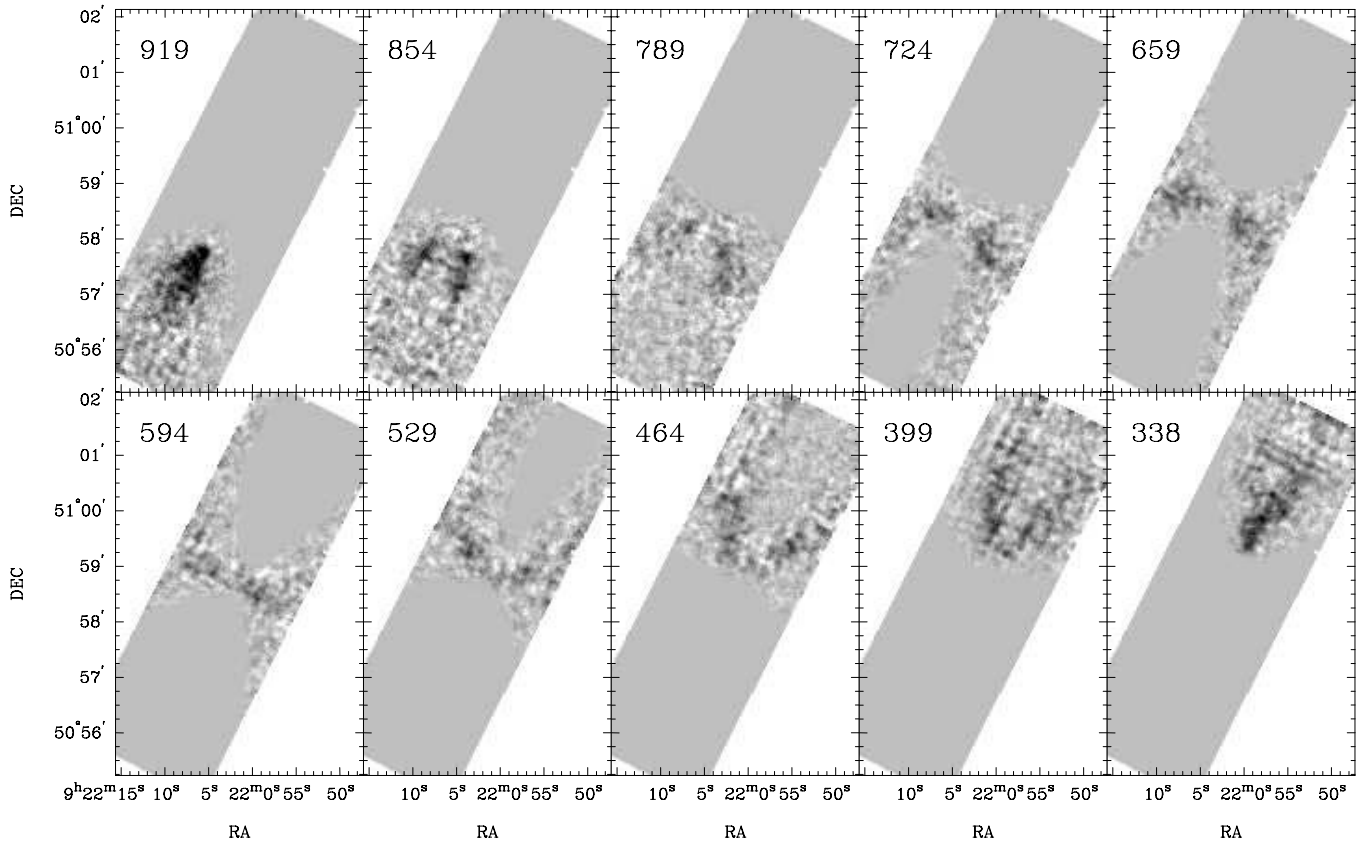


**Figure 5.** Channel maps for NGC 2841 at  $13''$  resolution. The gray-scale runs from  $-0.025$  to  $0.075$  K. Each channel is  $65 \text{ km s}^{-1}$  wide and the rms intensity in one channel is  $13 \text{ mK}$ . The smooth gray area indicates data at velocities outside the baseline fitting window, which are blanked during the reduction (Section 3.2).

values). Error bars show the uncertainty in the mean integrated intensity, derived by measuring the rms scatter within the tilted ring and dividing by  $\sqrt{N}$ , where  $N$  is the number of independent data points in the ring. Measurements with  $> 3\sigma$  significance appear as black circles, those with less as gray triangles.

Thick gray lines show exponential fits to the profiles, carried out over the region bracketed by the arrows at the top of each plot. The corresponding scale lengths, given in Table 3, span from  $0.8$  to  $3.2$  kpc. In most galaxies, an exponential decline captures the large-scale behavior well, though we cannot reliably fit NGC 2841 or NGC 4214. Studying BIMA SONG, which overlaps our sample, Regan et al. (2001) found the same variations in detailed morphology averaging into a common exponential decline. They discuss this topic in more detail. Both Regan et al. (2001) and Helfer et al. (2003) noted deviations from these fits in galaxy centers, which we also observe in the form of depressions (e.g., NGC 3521, NGC 7331) and excesses (e.g., NGC 3351, NGC 6946).

The exponential decline results from the combination of a decreasing filling fraction of CO emission and decreased intensity along individual lines of sight. To illustrate the relative contributions of these two effects, Figure 31 also shows the maximum integrated intensity inside each ring. Filled diamonds indicate rings where this maximum value is  $> 4\sigma$  and significantly ( $> 2\sigma$ ) larger than the absolute value of the minimum integrated intensity (roughly accounting for artifacts). Open diamonds show where the maximum intensity is below this value and we are correspondingly uncertain that the measurement is not biased by noise and artifacts. Comparing the two profiles, we observe a fairly close correspondence in the central parts

of galaxies and then a shallow decline in maximum intensity compared to average intensity at larger radii. The difference corresponds to the decreasing area subtended by bright CO emission.

Although H I typically dominates the ISM outside  $\sim 0.5r_{25}$ , we detect individual regions in the outskirts of several galaxies at high significance. In Figure 31 and Table 3, we report the largest radius at which we detect a “high signal spectrum.” We define this as a region with three consecutive velocity channels at  $> 3\sigma$  significance over 10 spatially contiguous pixels. This conservative definition generates no false positives in the whole survey when applied to the negative portions of the data. Figure 31 clearly shows that more extended, but lower significance, signal is present in many maps.

For the most part, these detections are simply associated with the outer part of the star-forming disk and can be clearly identified with structures seen in H I, UV, or IR maps that extend continuously from the inner to outer galaxy. This is the case for the detections at  $\sim 0.7$ – $1.0r_{25}$  in NGC 628, NGC 3521, NGC 5055, and NGC 6946 (the outer region in the latter corresponds to positions P10, 11, and 12 observed by Braine et al. 2007). The notable exception is the bright CO emission at  $1.33r_{25}$  in NGC 4736. This relatively narrow-line width feature is clearly visible in the channel map centered at  $405 \text{ km s}^{-1}$  in Figure 13. The emission is  $\sim 5'$  (projected distance of  $\sim 7$  kpc) from the center of the galaxy and well outside the main region of active star formation (e.g., see maps in Leroy et al. 2008). This feature matches the velocity and position of an H I filament outside the main body of the galaxy; it also shows UV and mid-IR ( $24 \mu\text{m}$ ) emission, indications of recent massive star formation.

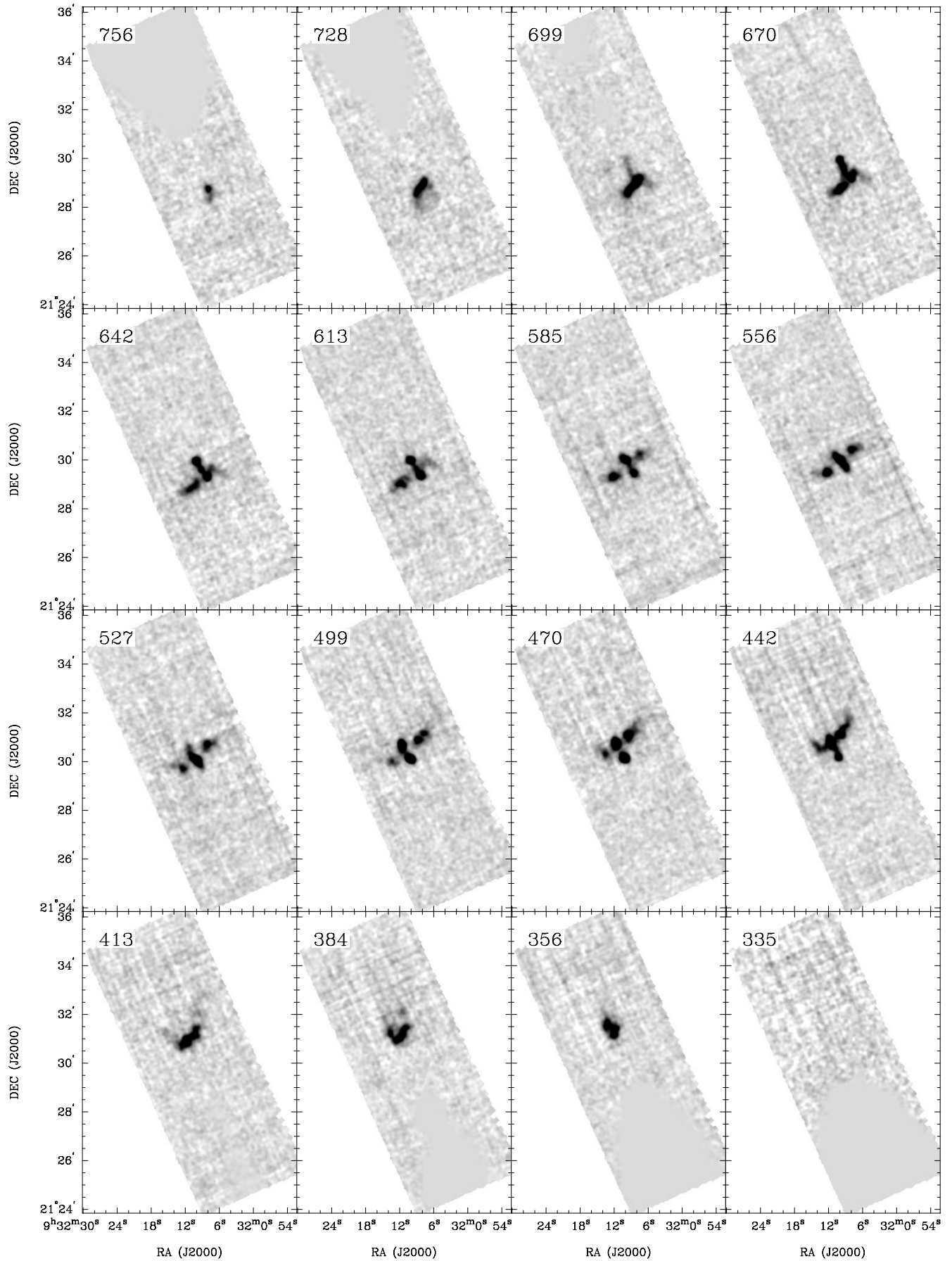


**Figure 6.** Channel maps for NGC 2903 at  $13''$  resolution. The gray-scale runs from  $-0.025$  to  $0.15$  K. Each channel is  $28.6$   $\text{km s}^{-1}$  wide and the rms intensity in one channel is  $10$  mK. The smooth gray area indicates data at velocities outside the baseline fitting window, which are blanked during the reduction (Section 3.2).

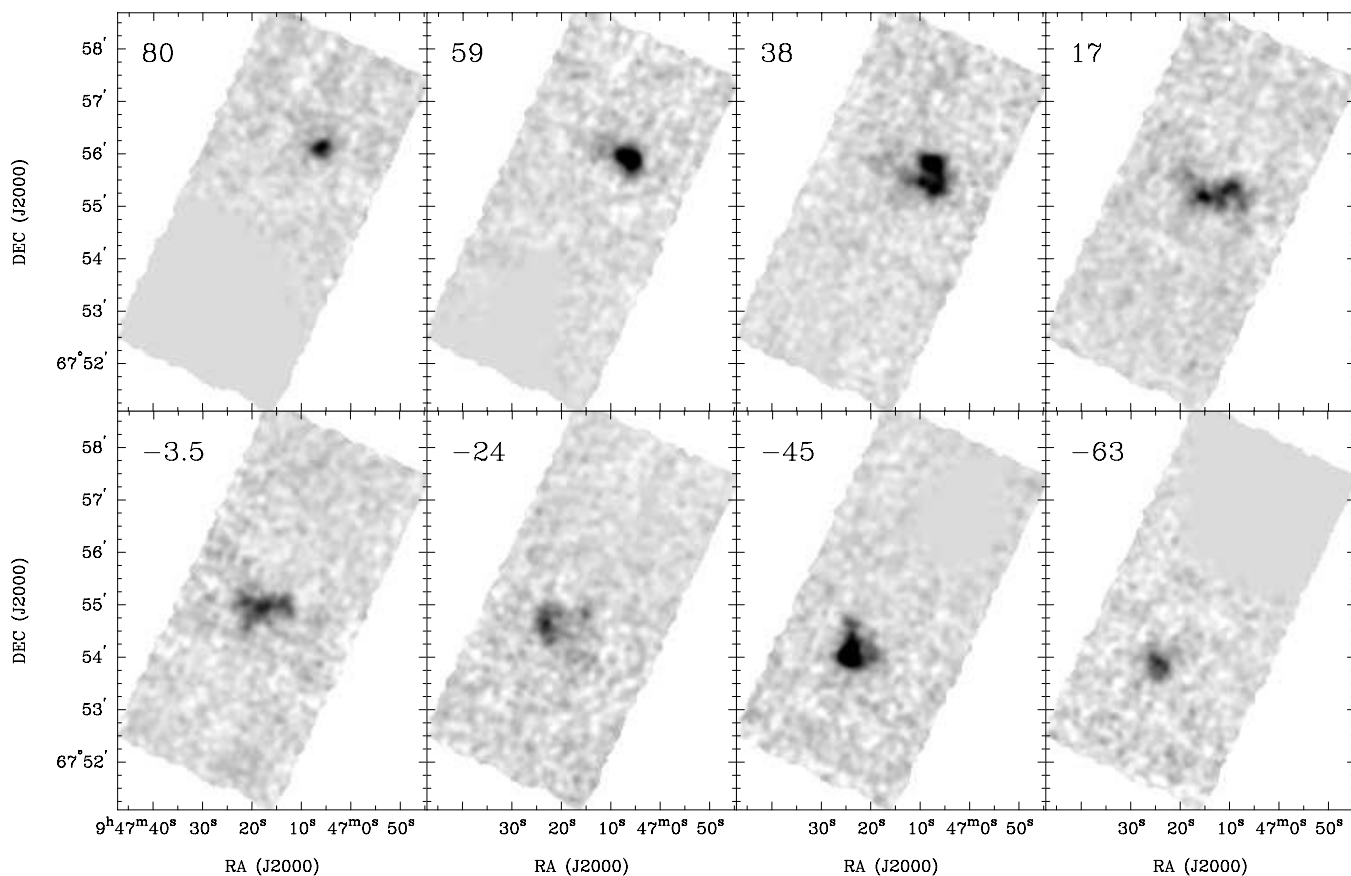


**Figure 7.** Channel maps for NGC 2976 at  $13''$  resolution. The gray-scale runs from  $-0.025$  to  $0.15$  K. Each channel is  $20.8 \text{ km s}^{-1}$  wide and the rms intensity in one channel is  $9 \text{ mK}$ . The smooth gray area indicates data at velocities outside the baseline fitting window, which are blanked during the reduction (Section 3.2).

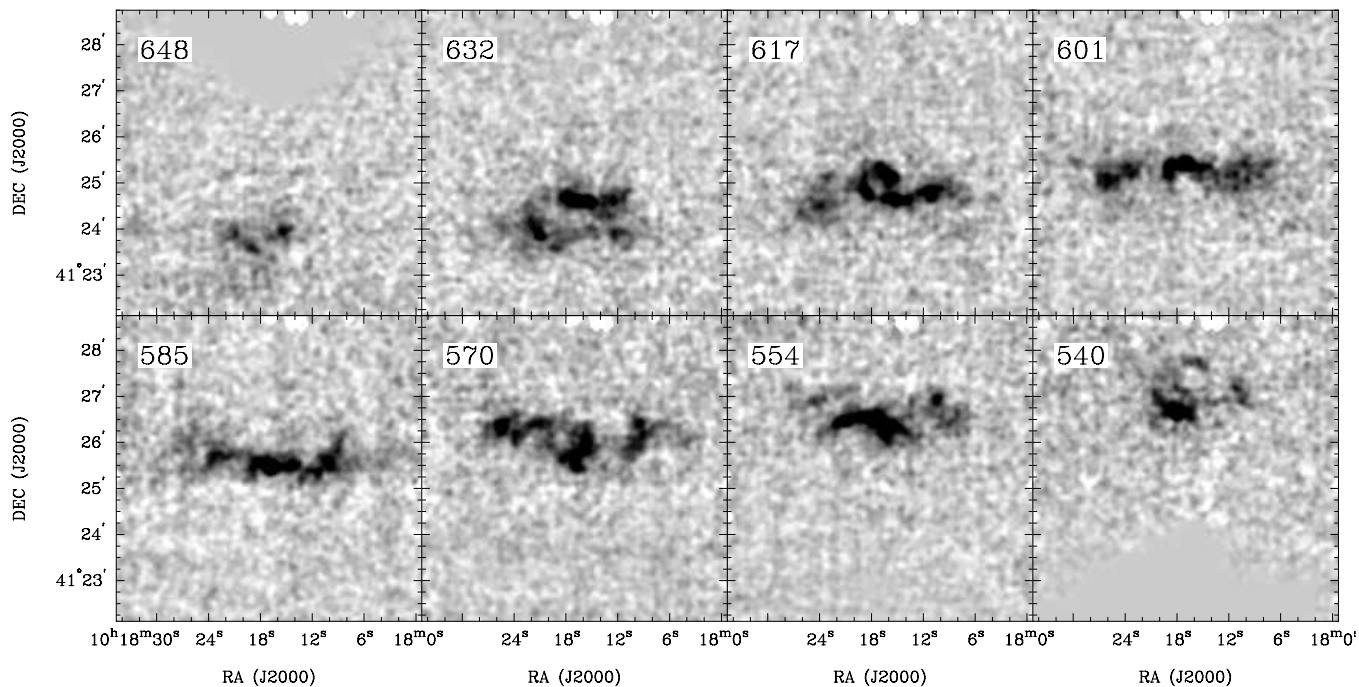


**Figure 8.** Channel maps for NGC 3184 at  $13''$  resolution. The gray-scale runs from  $-0.025$  to  $0.10$  K. Each channel is  $15.6 \text{ km s}^{-1}$  wide and the rms intensity in one channel is  $11 \text{ mK}$ . The smooth gray area indicates data at velocities outside the baseline fitting window, which are blanked during the reduction (Section 3.2).

### 4.3. Flux, Luminosity, and $H_2$ Mass

Columns 3 and 4 of Table 3 report the integrated CO flux and luminosity for each target, measured by summing the same

integrated intensity maps used to make the radial profiles. In all cases, the statistical uncertainty from Gaussian noise alone is small, meaning that the choice of area to integrate over, artifacts, and calibration of the telescope are the dominant sources of

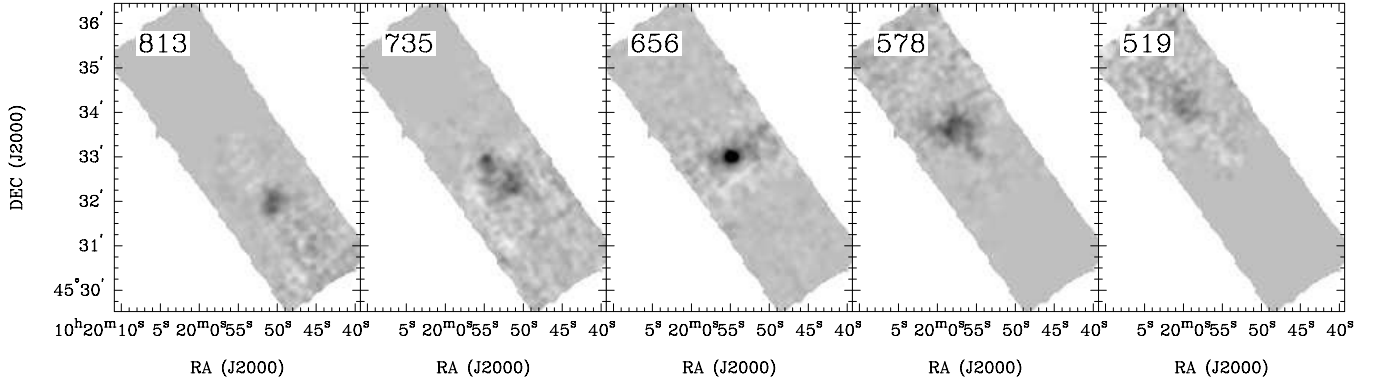


**Figure 9.** Channel maps for NGC 3198 at  $13''$  resolution. The gray-scale runs from  $-0.025$  to  $0.10$  K. Each channel is  $78.0$   $\text{km s}^{-1}$  wide and the rms intensity in one channel is  $4$  mK. The smooth gray area indicates data at velocities outside the baseline fitting window, which are blanked during the reduction (Section 3.2).

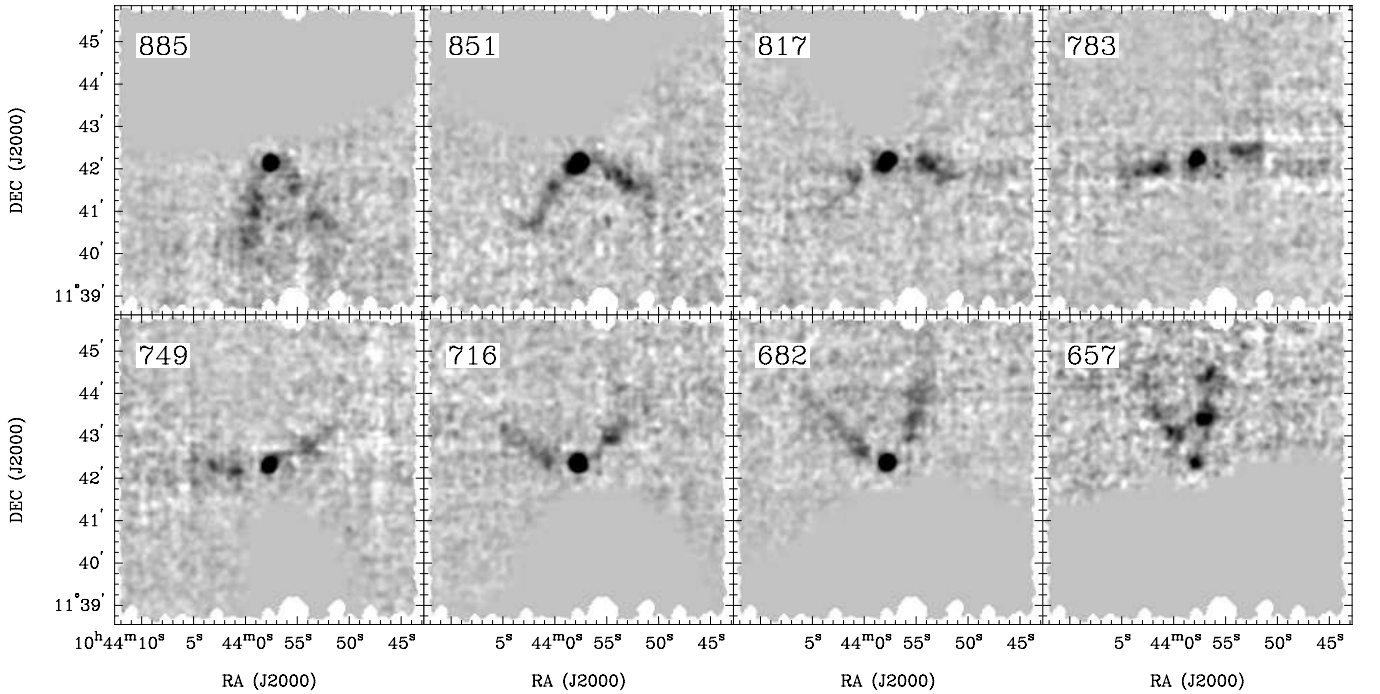


**Figure 10.** Channel maps for NGC 3351 at  $13''$  resolution. The gray-scale runs from  $-0.025$  to  $0.08$  K. Each channel is  $33.8$   $\text{km s}^{-1}$  wide and the rms intensity in one channel is  $7$  mK. The smooth gray area indicates data at velocities outside the baseline fitting window, which are blanked during the reduction (Section 3.2).

uncertainty. We estimate the uncertainty in the calibration at  $\sim 20\%$  (Section 3.5) and find that applying masking (e.g., as in Figures 17–30) alters the flux by  $\lesssim 15\%$  (slightly more in the cases of NGC 925, NGC 4214, and NGC 2841).

In four low metallicity dwarf irregulars (Holmberg I, Holmberg II, IC 2574, and DDO 154) we do not detect an extended distribution of CO. Instead, Table 3 gives upper limits on their CO content. To derive these, we create an integrated spectrum for each cube and estimate the rms noise at velocities offset from the H I line, regions expected to be signal free. Combining this rms noise with the H I line width ( $W_{20}$  from Walter et al. 2008) and area of the map yields the  $5\sigma$  upper limits on  $F_{\text{CO}}$  in Table 3. This approach takes into account the low-level correlated noise discussed in Section 3.5.

We quote CO flux,  $F_{\text{CO}}$ , in units of  $\text{K km s}^{-1} \text{arcsec}^2$  ( $T_{\text{MB}}$ ). This may be converted to  $\text{Jy km s}^{-1}$  via

$$F_{\text{CO}}[\text{Jy km s}^{-1}] = 0.036 F_{\text{CO}}[\text{K km s}^{-1} \text{arcsec}^2]. \quad (2)$$

We report CO luminosity,  $L_{\text{CO}}$ , in units of  $\text{K km s}^{-1} \text{pc}^2$  ( $T_{\text{MB}}$ ). This may be combined with a CO-to- $\text{H}_2$  conversion factor to

estimate the mass of molecular gas via

$$M_{\text{H}_2}[M_{\odot}] = 5.5 X_2 \frac{R_{21}}{0.8} L_{\text{CO}}[\text{K km s}^{-1} \text{pc}^2]. \quad (3)$$

Here  $X_2$  is the CO  $J = 1 \rightarrow 0$ -to- $\text{H}_2$  conversion factor normalized to  $2 \times 10^{20} \text{cm}^{-2} (\text{K km s}^{-1})^{-1}$ , approximately the solar neighborhood value (Strong & Mattox 1996; Dame et al. 2001).  $R_{21}$  is the CO  $J = 2 \rightarrow 1$  to  $J = 1 \rightarrow 0$  ratio; 0.8 is a typical value that we find comparing HERACLES to other surveys (Section 5.4.2). Equation (3) includes a factor of 1.36 to account for helium.

#### 4.4. GMC Filling Fraction and Point Source Sensitivity

In the Milky Way and nearby disk galaxies, CO emission is observed to come mostly from GMCs. These clouds have approximately constant surface densities,  $\Sigma_{\text{H}_2} \sim 170 M_{\odot} \text{pc}^{-2}$ , and brightness temperatures  $\gtrsim 4$  K (Solomon et al. 1987). We expect that these clouds similarly dominate the ISM across the disks of our sample.

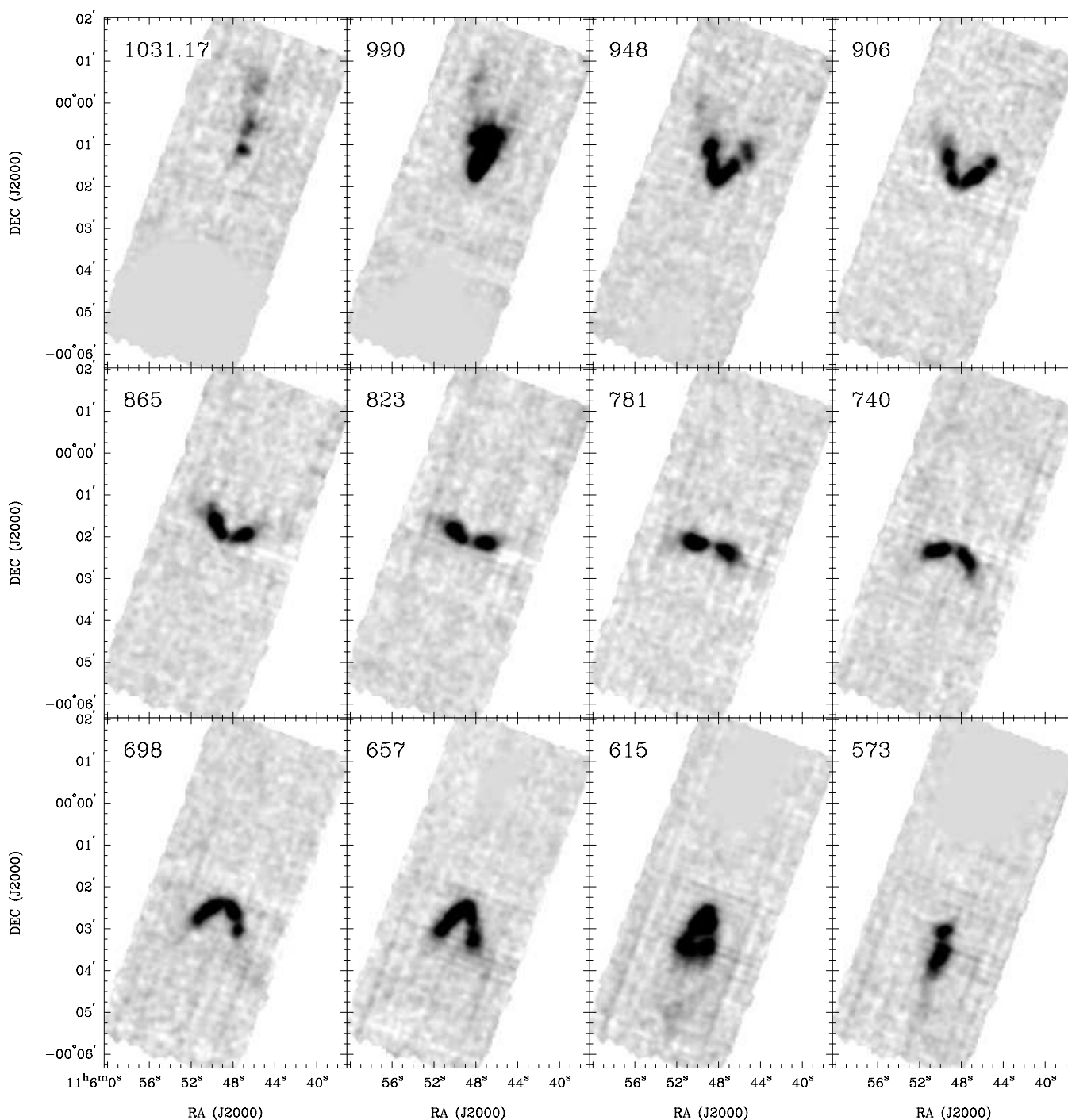


**Figure 11.** Channel maps for NGC 3521 at 13'' resolution. The gray-scale runs from  $-0.025$  to  $0.15$  K. Each channel is  $41.6 \text{ km s}^{-1}$  wide and the rms intensity in one channel is  $9 \text{ mK}$ . The smooth gray area indicates data at velocities outside the baseline fitting window, which are blanked during the reduction (Section 3.2).

The contrast between our measured surface densities and those of Galactic GMCs may give an idea of the filling factor of GMCs inside a resolution element. To translate CO intensity,  $I_{\text{CO}}$ , into molecular gas surface density,  $\Sigma_{\text{H}_2}$ , one can apply an analog of Equation (3),

$$\Sigma_{\text{H}_2} [M_{\odot} \text{ pc}^2] = 5.5 X_2 \frac{R_{21}}{0.8} I_{\text{CO}} [\text{K km s}^{-1}]. \quad (4)$$

The contours in Figures 21–34 thus correspond to  $\Sigma_{\text{H}_2} \approx 5.5$  (gray), 11 (first black), 22, 44, 88, 176 (first white)  $M_{\odot} \text{ pc}^{-2}$ , and so on, values that can be explained if  $\sim 3, 6, 13, 25, 50,$  and

100% of the area inside the beam is covered by Galactic GMCs. Most area where we see CO emission has relatively low filling factors,  $\sim 5\%–15\%$ .

The peak intensity maps allow a similar comparison. If  $\sim 4 \text{ K}$  is the typical brightness for a Galactic cloud,  $T_{\text{peak}} = 0.1$  and  $0.5 \text{ K}$ —values that bracket most of the observed peak temperatures—correspond to filling factors of  $\sim 3$  and  $13\%$ .

The point mass sensitivity of our maps corresponds to a collection of several Galactic GMCs. For a source with full line width of  $\sim 10.4 \text{ km s}^{-1}$  (typical for Galactic GMCs, Solomon et al. 1987), our typical rms sensitivity translates to a  $3\sigma$  point

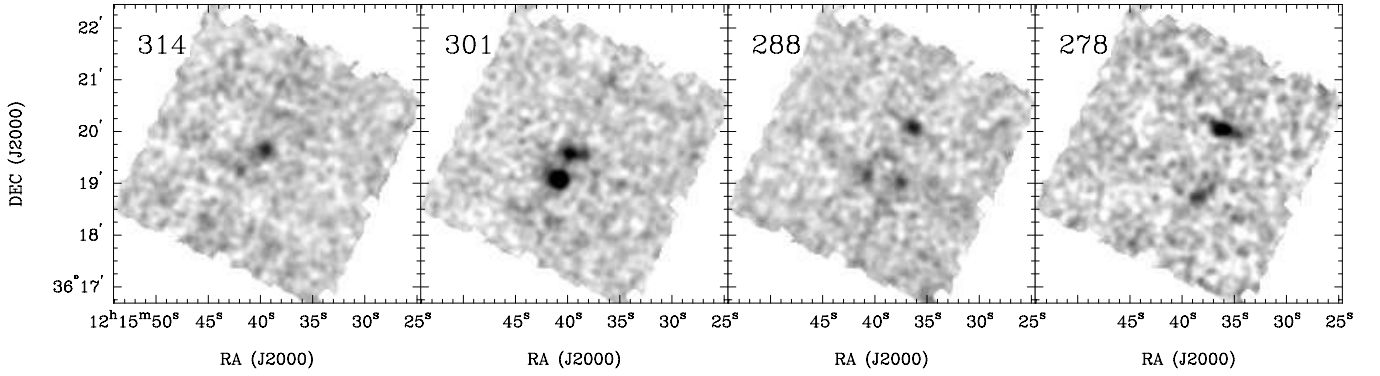


**Figure 12.** Channel maps for NGC 4214 at  $13''$  resolution. The gray-scale runs from  $-0.025$  to  $0.1$  K. Each channel is  $13.0 \text{ km s}^{-1}$  wide and the rms intensity in one channel is  $10 \text{ mK}$ . The smooth gray area indicates data at velocities outside the baseline fitting window, which are blanked during the reduction (Section 3.2).

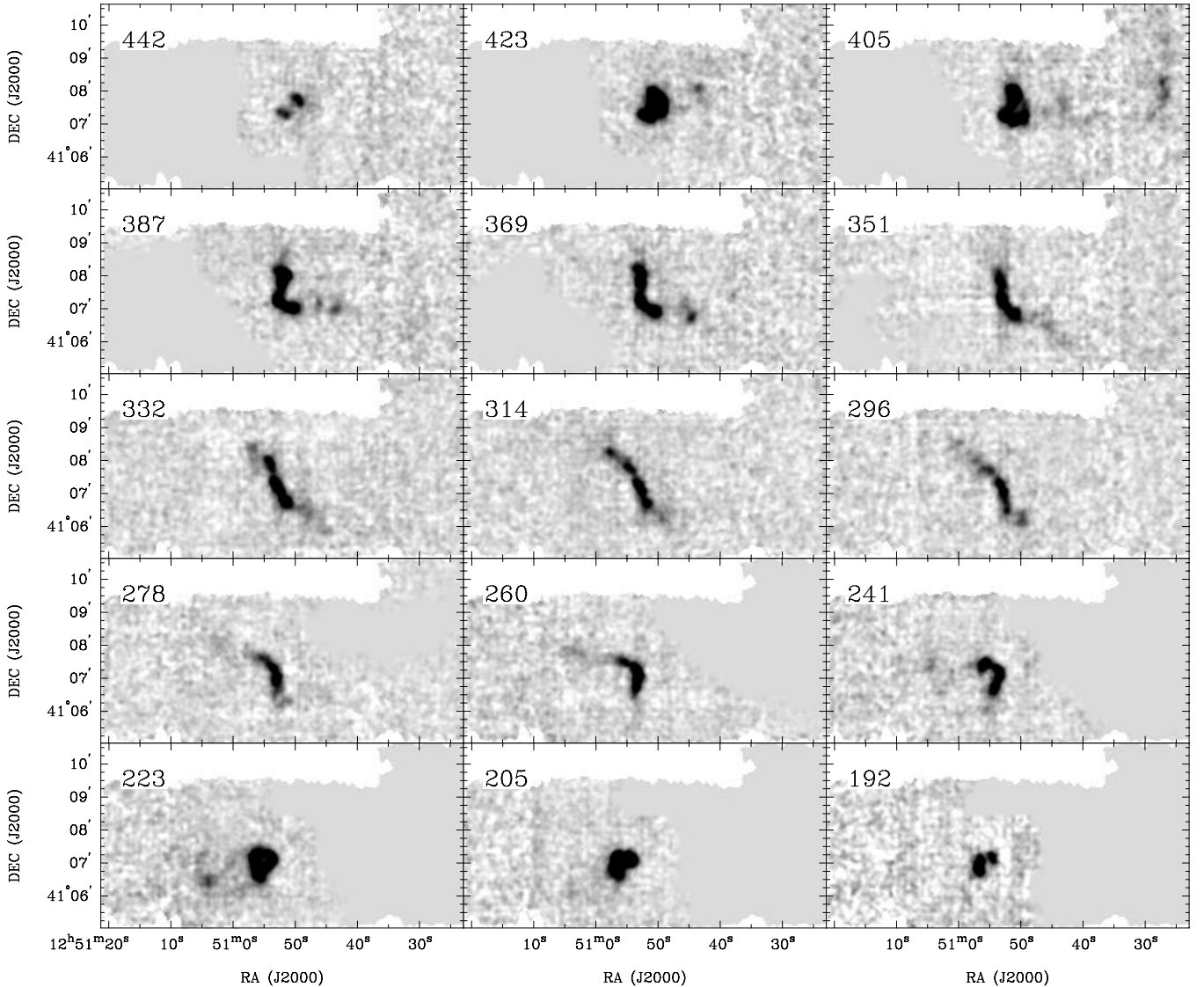


**Figure 13.** Channel maps for NGC 4736 at  $13''$  resolution. The gray-scale runs from  $-0.025$  to  $0.15$  K. Each channel is  $18.2 \text{ km s}^{-1}$  wide and the rms intensity in one channel is  $12 \text{ mK}$ . The smooth gray area indicates data at velocities outside the baseline fitting window, which are blanked during the reduction (Section 3.2).

source sensitivity of  $4.8 \times 10^5 d_{10} \text{ K km s}^{-1} \text{ pc}^2$ , where  $d_{10}$  is the distance to the source divided by  $10 \text{ Mpc}$ . From Equation (4), this corresponds to an  $\text{H}_2$  mass of  $2.7 \times 10^6 d_{10} M_\odot$ , which is near the high end found for Galactic GMCs (clouds with masses  $10^5$ – $10^6 M_\odot$  account for most of the Galactic  $\text{H}_2$ , e.g., Blitz

1993). For reference, the most massive Milky Way GMC, the most massive cloud detected in M33, and the Orion molecular complex have masses of  $\sim 6 \times 10^6 M_\odot$ ,  $\sim 7 \times 10^5 M_\odot$ , and  $\sim 5 \times 10^5 M_\odot$ , respectively (Solomon et al. 1987; Engargiola et al. 2003; Wilson et al. 2005).

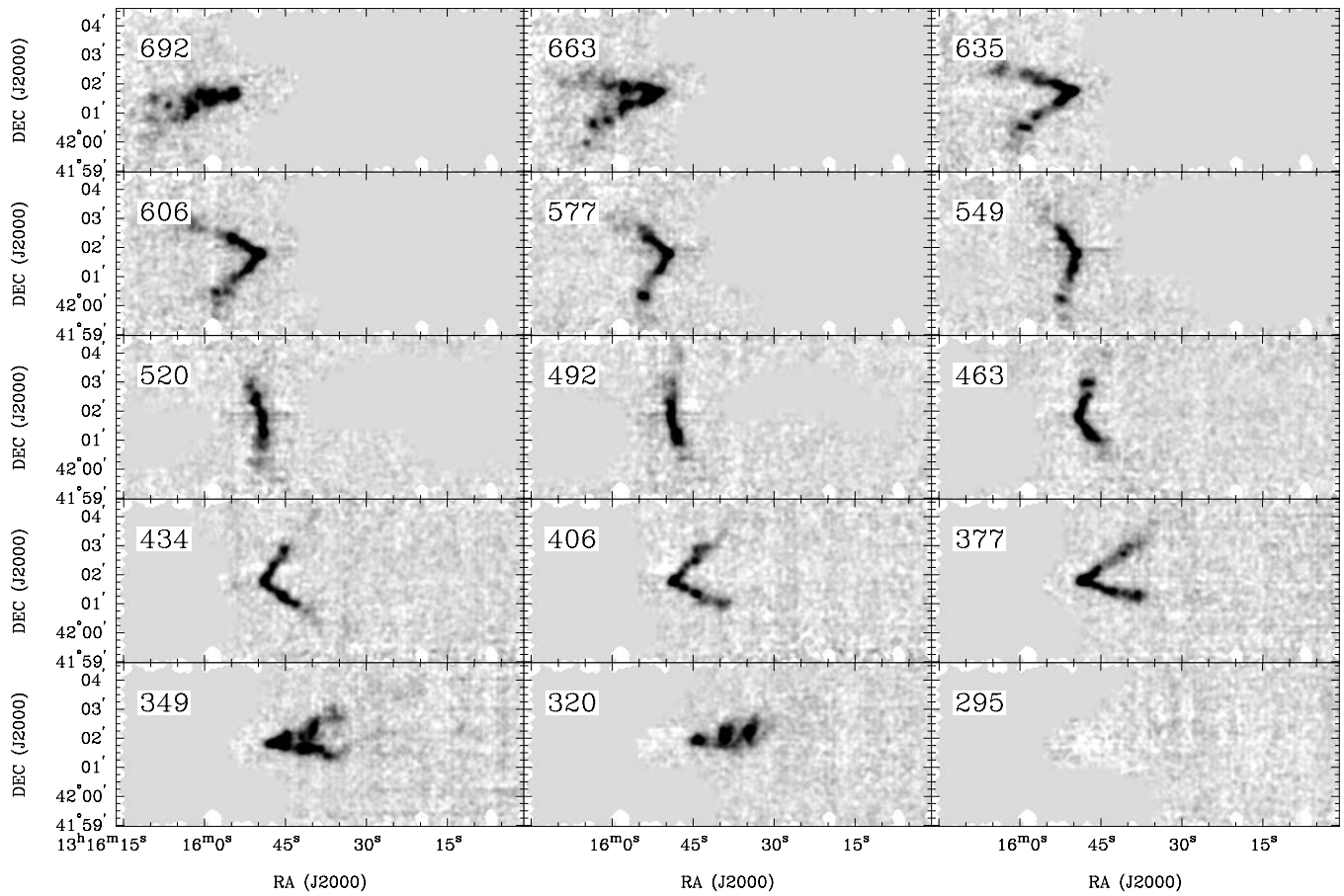


**Figure 14.** Channel maps for NGC 5055 at  $13''$  resolution. The gray-scale runs from  $-0.025$  to  $0.15$  K. Each channel is  $28.6 \text{ km s}^{-1}$  wide and the rms intensity in one channel is  $10 \text{ mK}$ . The smooth gray area indicates data at velocities outside the baseline fitting window, which are blanked during the reduction (Section 3.2).

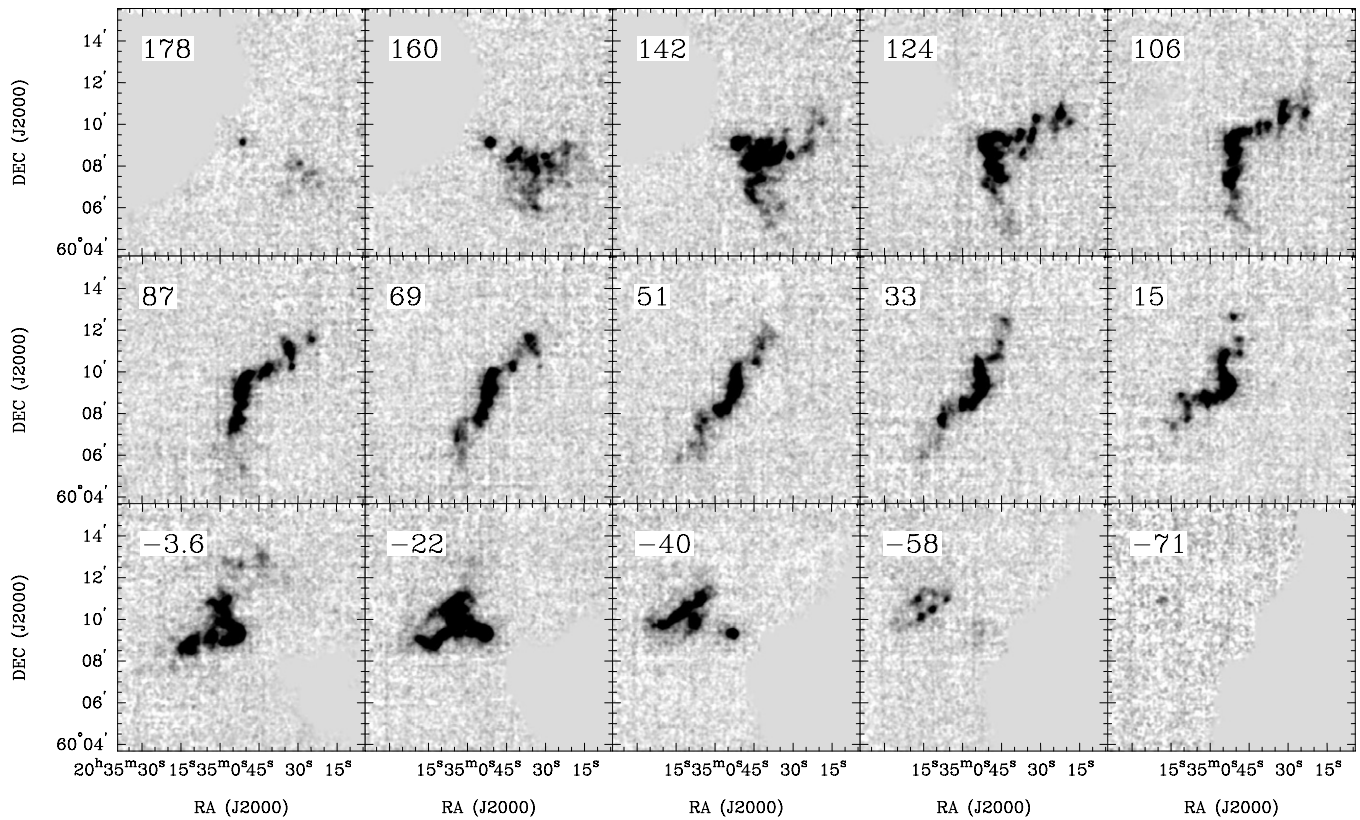


**Figure 15.** Channel maps for NGC 6946 at  $13''$  resolution. The gray-scale runs from  $-0.025$  to  $0.15$  K. Each channel is  $18.2 \text{ km s}^{-1}$  wide and the rms intensity in one channel is  $13 \text{ mK}$ . The smooth gray area indicates data at velocities outside the baseline fitting window, which are blanked during the reduction (Section 3.2).

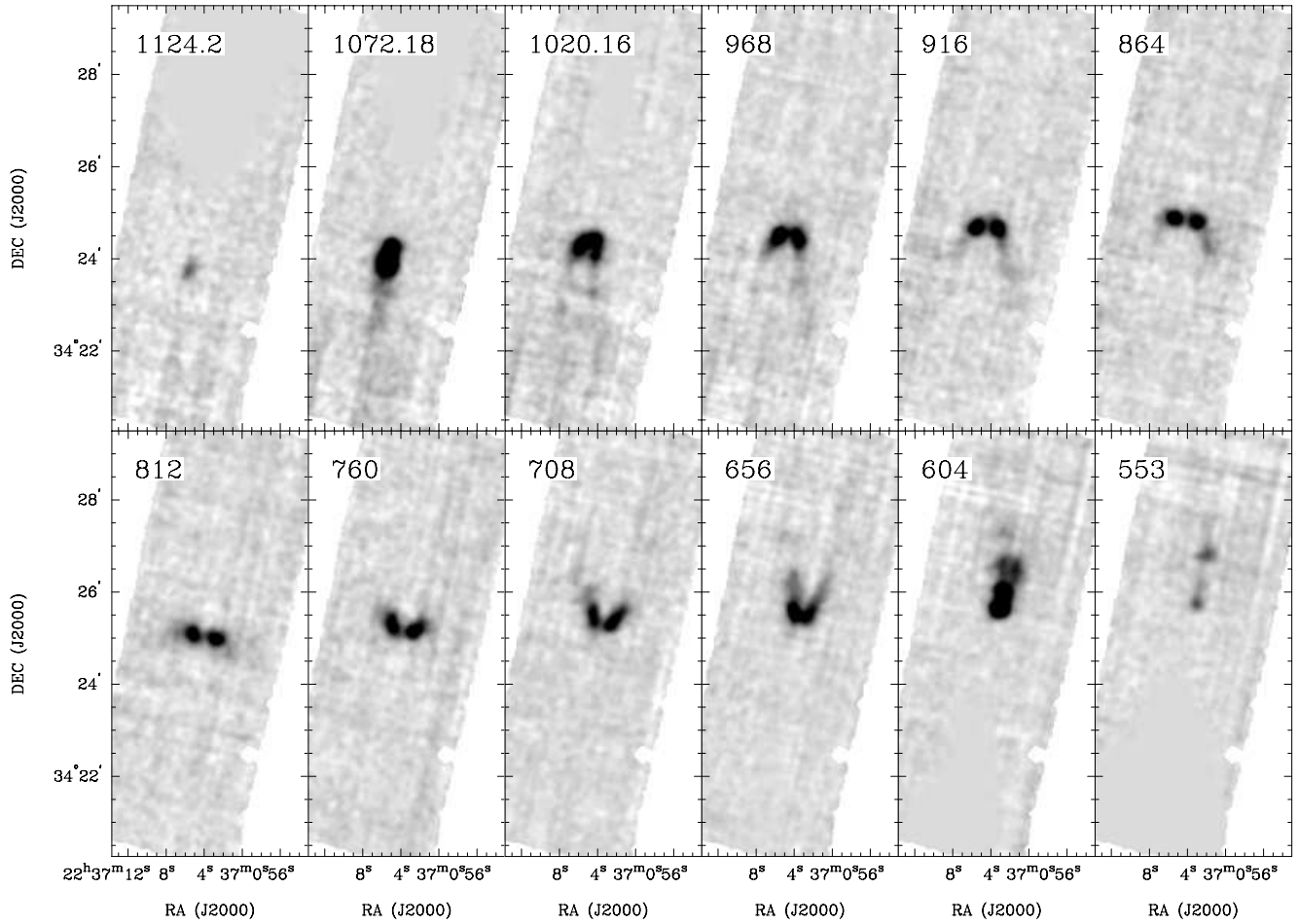


**Figure 16.** Channel maps for NGC 7331 at 13'' resolution. The gray-scale runs from  $-0.025$  to  $0.15$  K. Each channel is  $52.0 \text{ km s}^{-1}$  wide and the rms intensity in one channel is  $8 \text{ mK}$ . The smooth gray area indicates data at velocities outside the baseline fitting window, which are blanked during the reduction (Section 3.2).

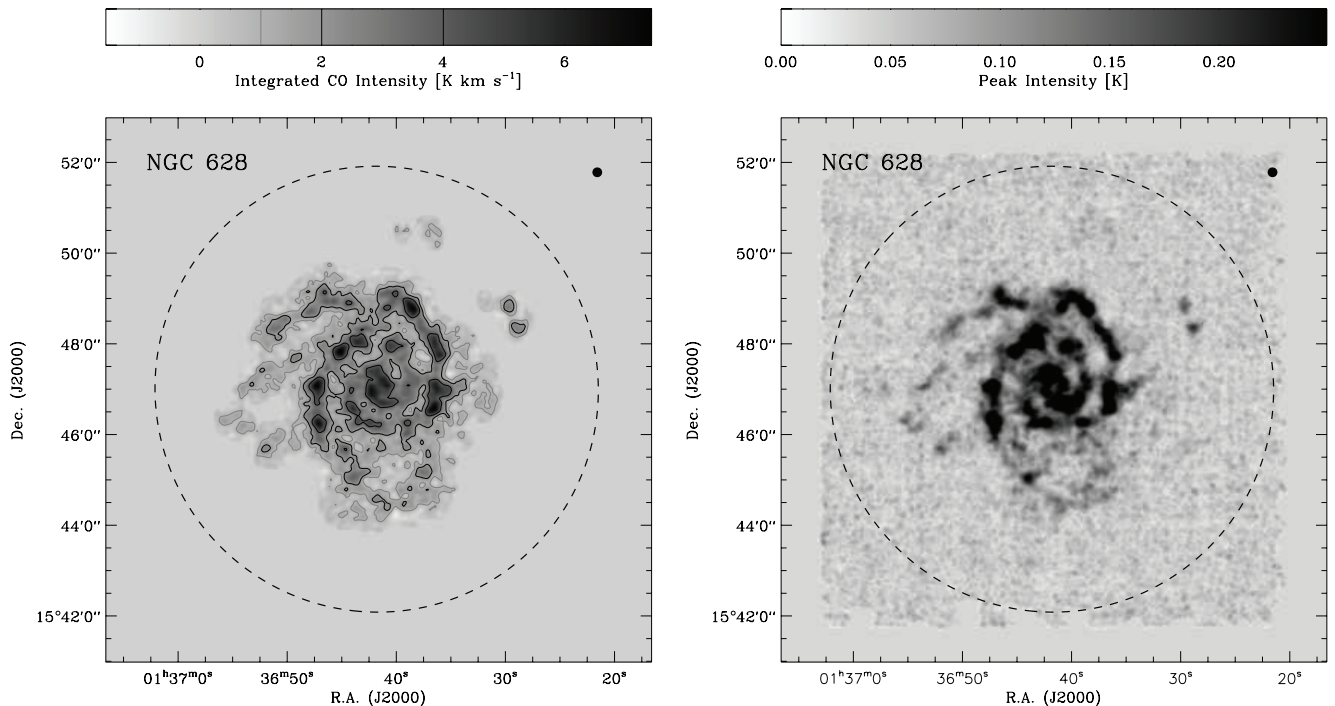


**Figure 17.** Left: integrated intensity CO  $J = 2 \rightarrow 1$  intensity along each line of sight, summing over regions where  $I_{\text{CO}} > 2\sigma$  in consecutive channel maps (see the text). Contours begin at  $1 \text{ K km s}^{-1}$  and increase by a factor of 2 each step. The first black contour indicates  $2 \text{ K km s}^{-1}$  and the first white contour shows  $32 \text{ K km s}^{-1}$ , which correspond approximately to surface densities of 11 and  $176 M_{\odot} \text{ pc}^{-2}$ . In both figures a dashed ellipse shows  $r_{25}$ , the 25th magnitude isophote, and a solid black circle indicates the  $13''$  angular resolution of the data. Right: peak CO  $J = 2 \rightarrow 1$  intensity along each line of sight for NGC 628.

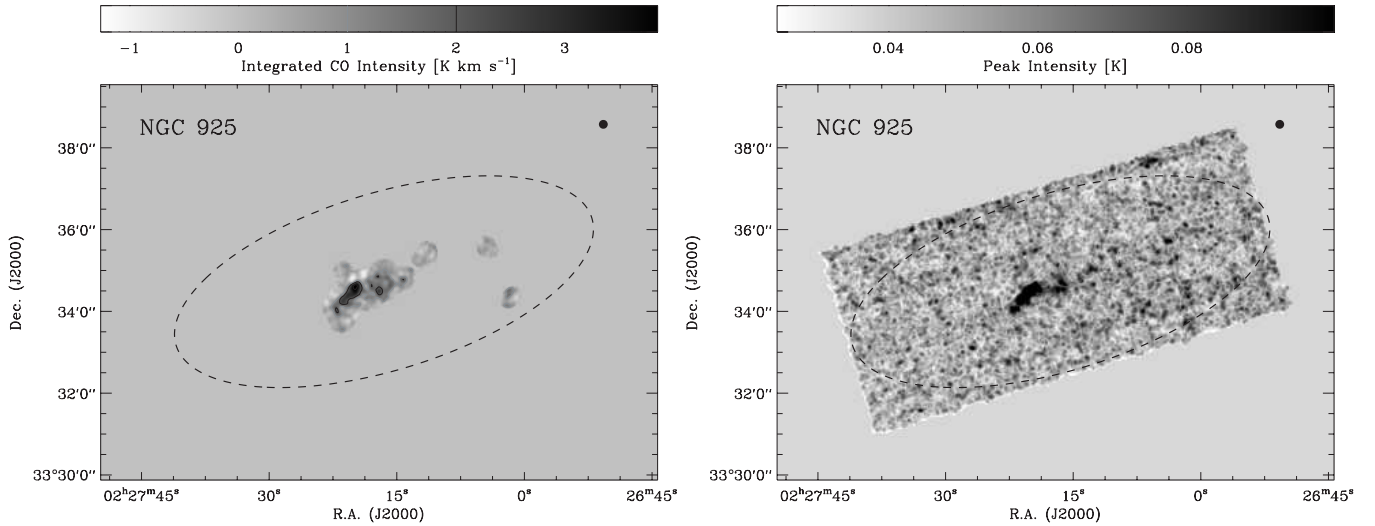


Figure 18. As Figure 17 but for NGC 925.

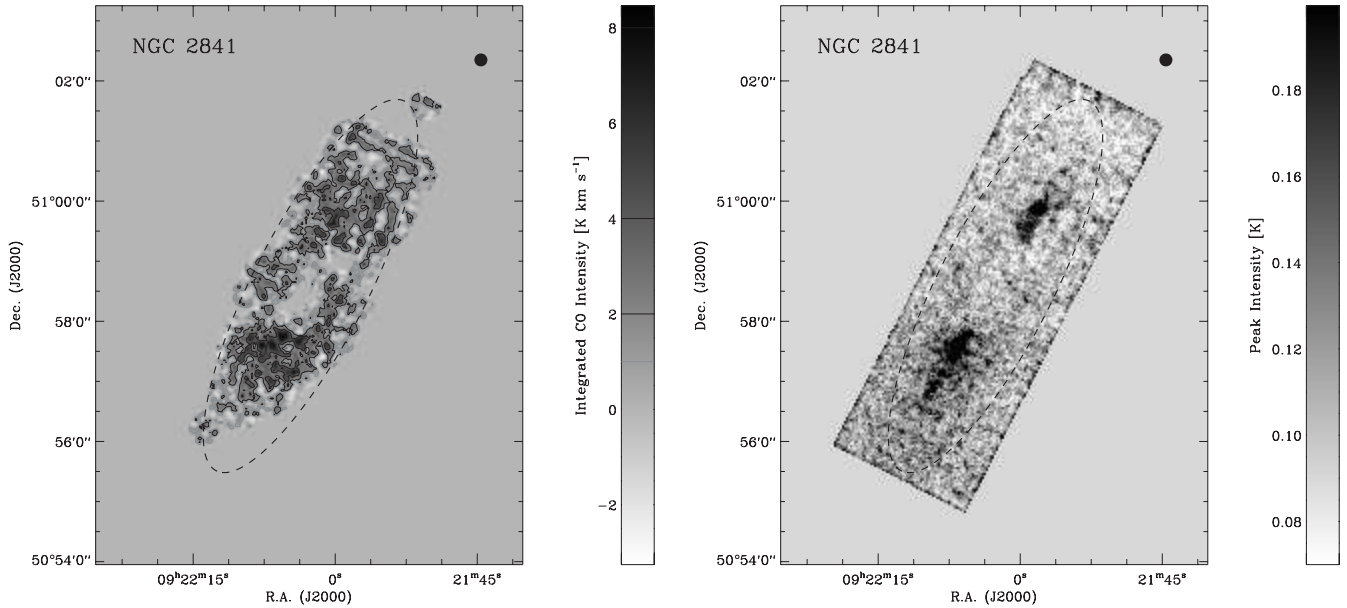


Figure 19. As Figure 17 but for NGC 2841.

## 5. COMPARISON WITH OTHER DATA

Previous observations of our targets at wavelengths from radio to UV allow a range of comparisons. Here we use these data to calculate the  $H_2$ -to- $H I$  and  $H_2$ -to-stellar mass ratio, to test our assumption that  $H I$  and  $CO$  exhibit the same mean velocity, to check our observations against previous  $CO$  measurements, and to estimate the  $CO J = 2 \rightarrow 1/1 \rightarrow 0$  line ratio. More detailed comparisons to  $H I$ , IR, and UV data may be found in Leroy et al. (2008) and Bigiel et al. (2008).

### 5.1. Relative Masses of $H_2$ , $H I$ , and Stars

Columns 7, 8, and 9 in Table 3 list the ratios of  $H_2$  mass to  $H I$  mass ( $M_{H_2}/M_{H I}$ ),  $H_2$  mass to stellar mass ( $M_{H_2}/M_*$ ), and gas to stellar mass ( $(M_{H_2} + M_{H I})/M_*$ ) for each galaxy. We adopt  $M_{H I}$  from Walter et al. (2008), scaling by 1.36 to account for helium. The stellar masses are taken from Leroy et al. (2008), who estimate them from SINGS  $3.6 \mu m$  imaging assuming a Kroupa IMF (NGC 2903 comes from de Blok et al. 2008). de

Blok et al. (2008) investigate possible variations in the  $3.6 \mu m$  mass-to-light ratio and find a factor of 2 plausible.

The range of  $M_{H_2}/M_*$  is 0.01–0.25, with most values between 0.03 and 0.1.  $M_{H_2}/M_{H I}$  spans from 0.02 to 1.13, with most targets in the range  $\sim 0.2$ –0.6 (in our sample only NGC 4736 appears to have more  $H_2$  than  $H I$ ). Combined, these ratios yield a wide range of gas-richness, from  $(M_{H I} + M_{H_2})/M_* \sim 0.2$  in relatively early type spirals to  $\gtrsim 3$  in our late-type, low-mass nondetections.

### 5.2. Scale Lengths At Other Wavelengths

Figure 32 shows the size of our galaxies at other wavelengths as a function of the exponential scale lengths that we measure from azimuthally averaged  $CO$  profiles,  $l_{CO}$ . Filled circles show  $0.2r_{25}$ , which Young et al. (1995) found to be a typical scale length of  $CO$  emission. We observe the same here,  $l_{CO} = 0.2r_{25}$  with a  $1\sigma$  scatter of 0.05. Stars show the exponential scale length fit to median profiles of  $3.6 \mu m$  emission (from Leroy et al. 2008), a tracer of the distribution of old stellar mass.

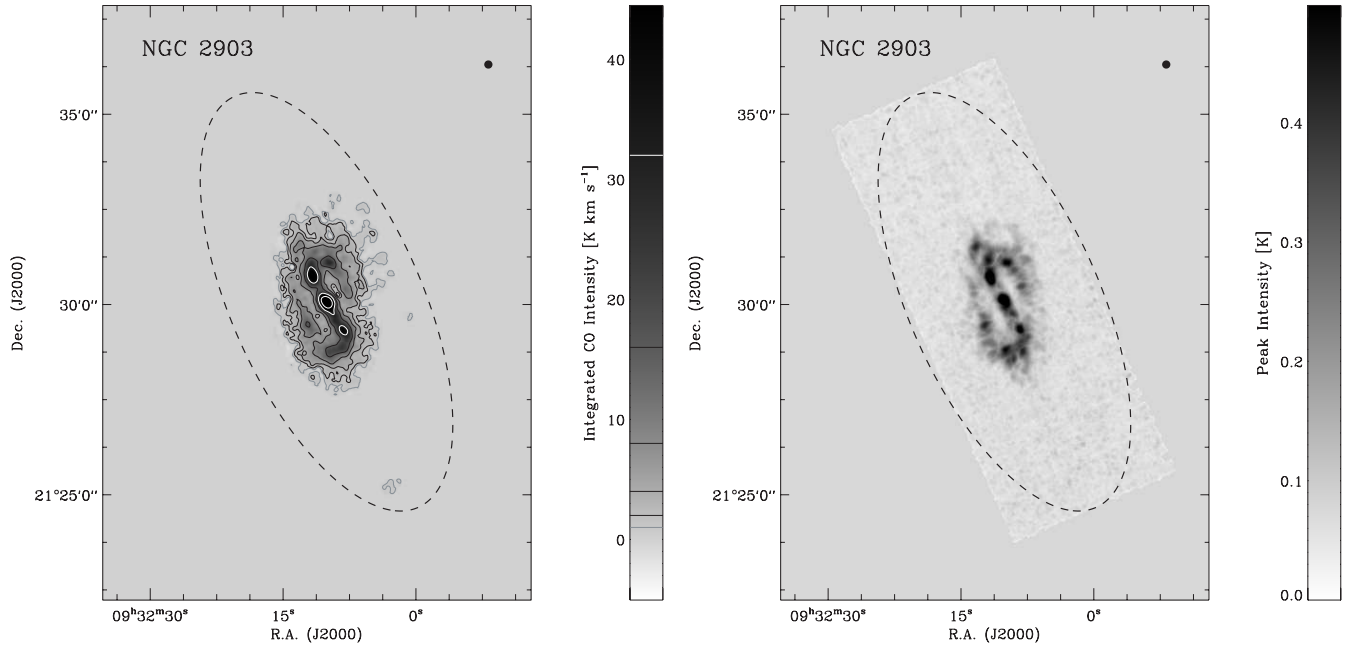


Figure 20. As Figure 17 but for NGC 2903.

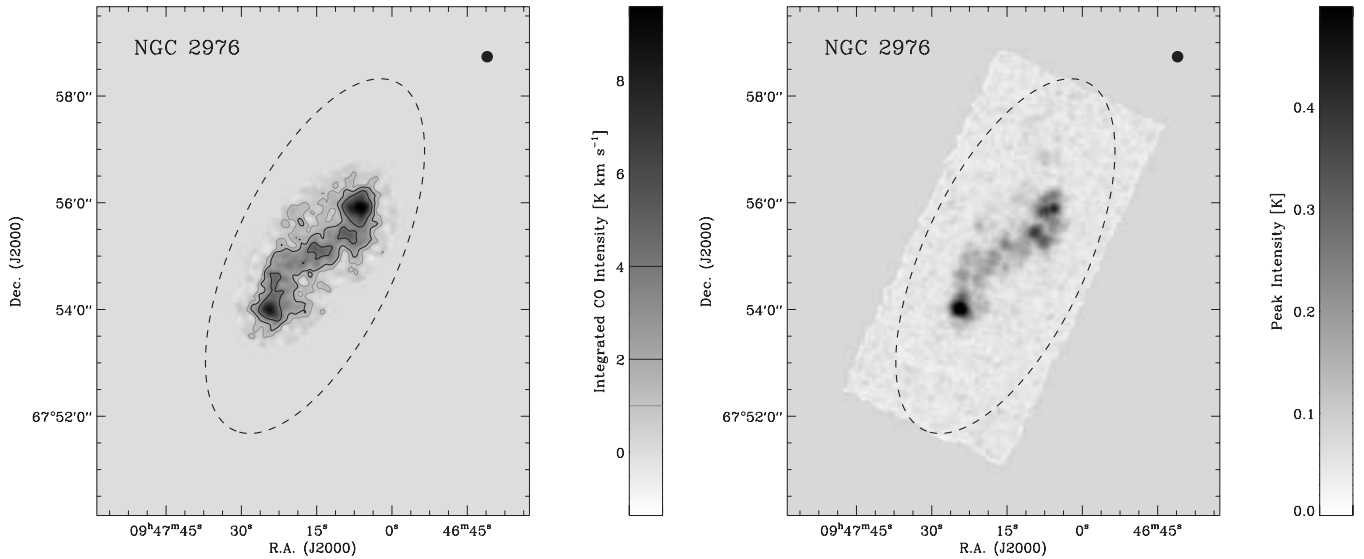


Figure 21. As Figure 17 but for NGC 2976.

Diamonds plot the exponential scale length fit to profiles of star formation surface density, estimated from a combination of *Galaxy Evolution Explorer* (GALEX) FUV emission and *Spitzer* 24  $\mu\text{m}$  data (from Leroy et al. 2008). All three quantities scatter about equally, with  $I_{\text{CO}}$  on average  $\sim 5\%$ – $10\%$  lower than the other two, not a significant difference. The plot underscores the well-established close association between CO emission and stellar light in disk galaxies (e.g., Young & Scoville 1991; Young et al. 1995; Regan et al. 2001) and the similar match between the distributions of CO and star formation (e.g., Leroy et al. 2008).

### 5.3. HERACLES CO and THINGS H I Velocities

The THINGS data allow us to test our assumption that CO and H I have the same mean velocity (Section 3.2). To do so, we assemble a set of  $\sim 1200$  spatially independent spectra, each with peak SNR greater than 5. For each spectrum, we measure the

intensity-weighted mean velocity of CO  $J = 2 \rightarrow 1$  emission,  $\langle v_{\text{CO}} \rangle$ , and extract the intensity-weighted mean H I velocity,  $\langle v_{\text{HI}} \rangle$ , from the THINGS first moment maps (Walter et al. 2008).

The gray histogram in Figure 33 shows the distribution of  $\langle v_{\text{CO}} \rangle - \langle v_{\text{HI}} \rangle$  for all 1200 spectra. The mean velocities of CO and H I appear closely matched for most spectra. A Gaussian fit to the distribution (thick dashed line) has  $1\sigma$  width  $5.9 \text{ km s}^{-1}$  and a center consistent with zero offset ( $-0.05 \text{ km s}^{-1}$ ). The scatter in  $\langle v_{\text{CO}} \rangle - \langle v_{\text{HI}} \rangle$  is much smaller than the 60–300  $\text{km s}^{-1}$  width of our baseline fitting regions (Section 3.2), so the agreement is not a product of our reduction. The extended wings come almost entirely from a few inclined, massive spirals (NGC 2841, 2903, 3521, 7331), galaxies that also sometimes show multiple components in a single H I spectrum. These outliers are interesting, but here we emphasize the basic result that H I and CO gas show approximately the same mean velocity.

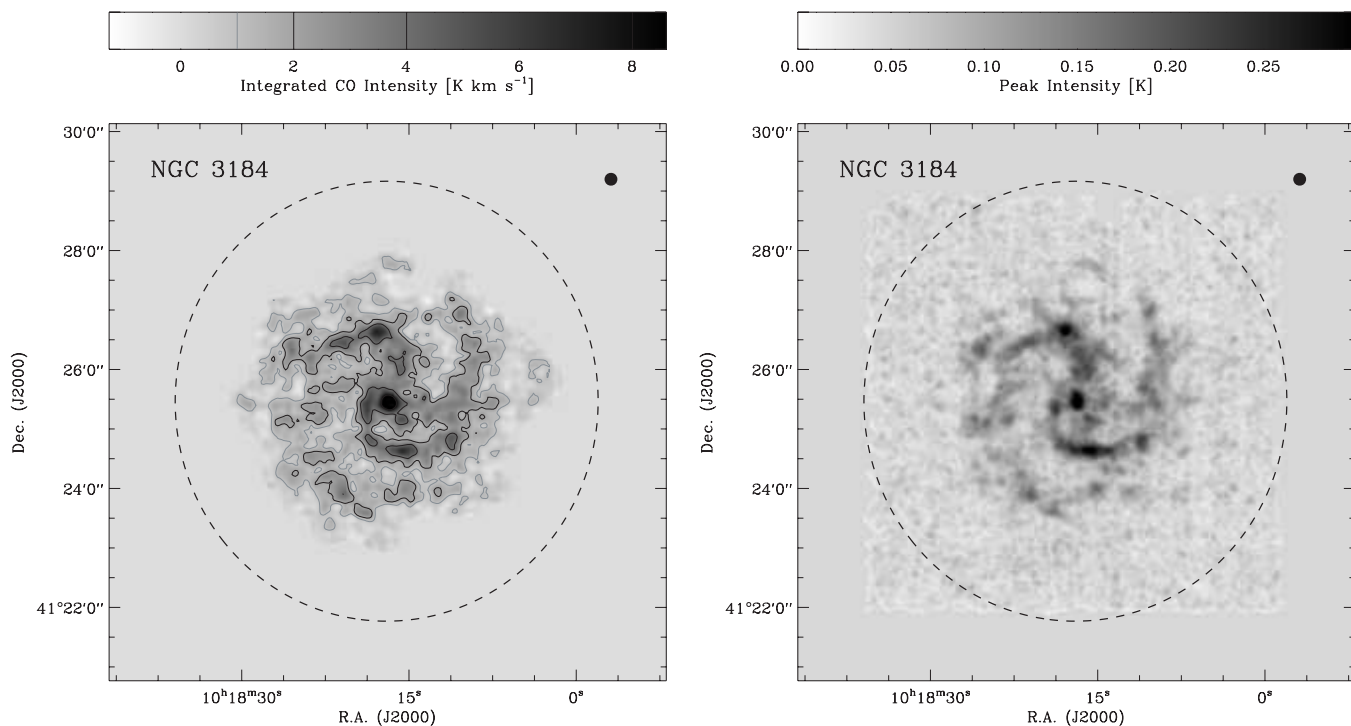


Figure 22. As Figure 17 but for NGC 3184.

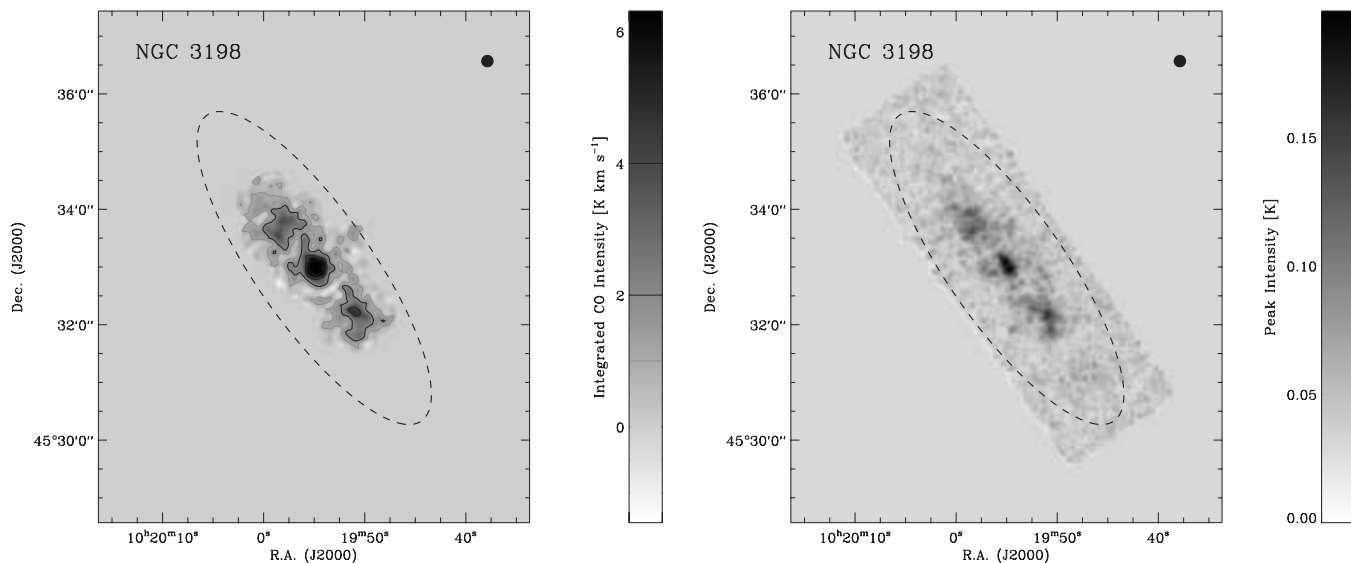


Figure 23. As Figure 17 but for NGC 3198.

#### 5.4. Comparison to CO $J = 1 \rightarrow 0$ Observations

CO  $J = 1 \rightarrow 0$  emission has been mapped for many galaxies in our sample. Here we compare HERACLES to the FCRAO survey (Young et al. 1995, resolution  $45''$ ), BIMA SONG (Helfer et al. 2003), and the Nobeyama CO Atlas of Nearby Spiral Galaxies (Kuno et al. 2007, resolution  $15''$ ). We use two data sets drawn from BIMA SONG: on-the-fly maps made with the NRAO 12 m (resolution  $55''$ ) and the combined BIMA + 12 m data (typical resolution  $\sim 6''$ ). We refer to the former as the “NRAO 12 m” and the latter as BIMA SONG.

Our method of comparison is the following:

1. We convolve each plane of each HERACLES data cube with a series of Gaussian kernels to create data cubes with angular resolutions of 15, 45, and  $55''$ , appropriate for comparison with Kuno et al. (2007), the FCRAO survey, and the NRAO 12 m data. We convolve BIMA SONG to  $15''$  resolution in the same manner and compare it to HERACLES at this resolution.
2. For each galaxy, we extract spectra from each data cube at a series of independent pointings. When comparing to the FCRAO survey, these are the FCRAO pointings, which are usually spaced by a full ( $45''$ ) beam width along the major axis. When comparing with Kuno et al. (2007), BIMA SONG, and the NRAO 12 m, the pointings are on a grid that covers most of the galaxy with sampling points spaced by a full beam width—i.e.,  $15''$  and  $55''$ .
3. We smooth these spectra in velocity so that they all have comparable velocity resolution,  $\sim 15 \text{ km s}^{-1}$  (chosen to match the FCRAO survey).

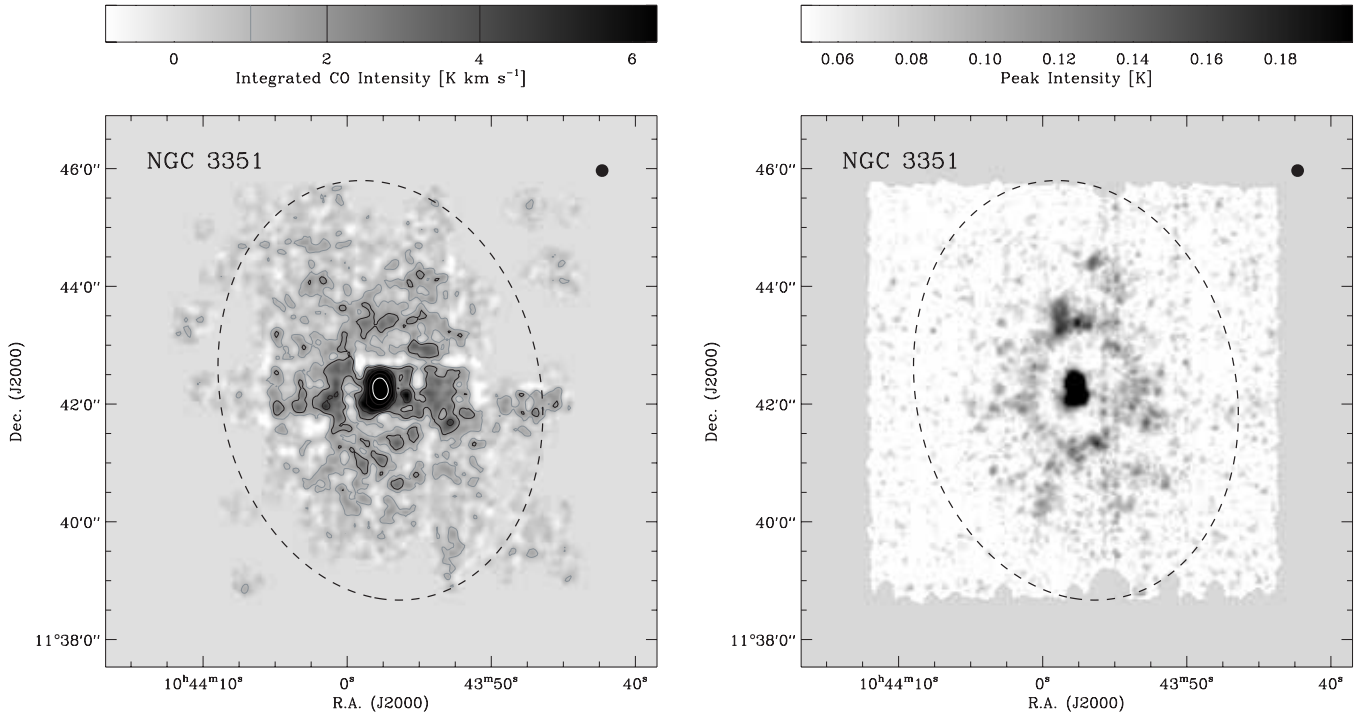


Figure 24. As Figure 17 but for NGC 3351.

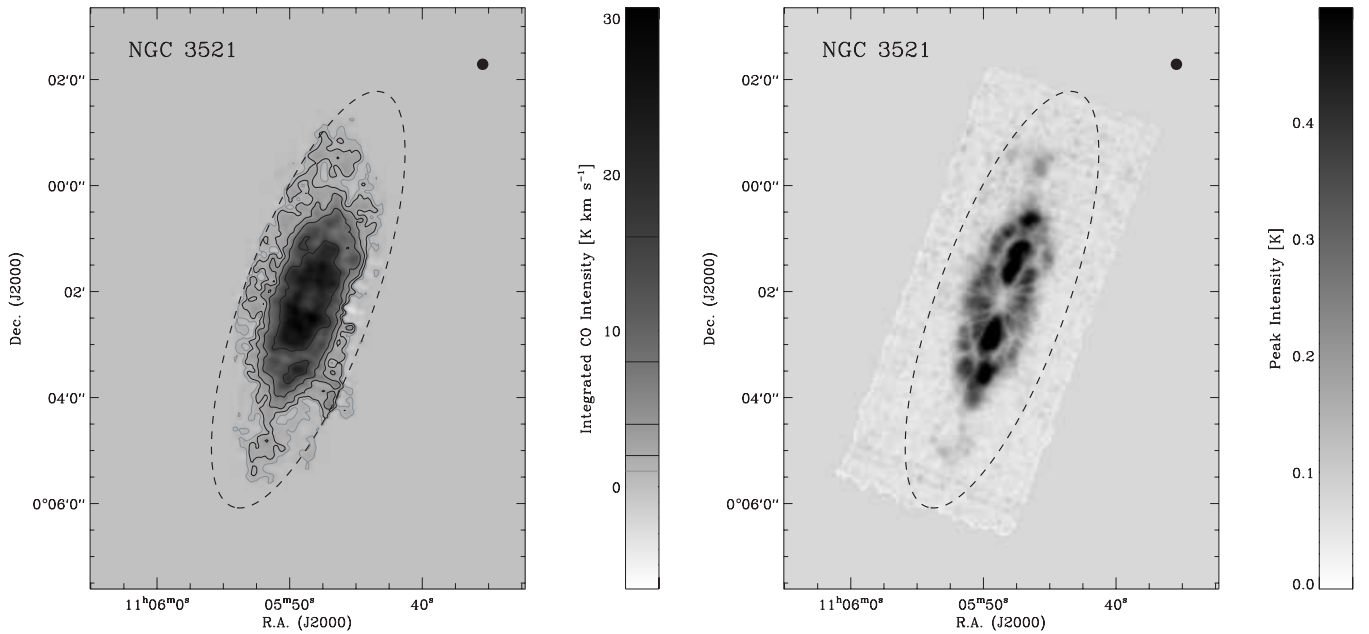


Figure 25. As Figure 17 but for NGC 3521.

4. We discard all spectra where the peak SNR is less than 5. When comparing with the FCRAO survey, we consider only pointings where Young et al. (1995) report a peak temperature, mean velocity, and line width.

The result is a series of reasonably high SNR spectra at matched positions with matching angular and velocity resolutions. For each spectrum, we measure four parameters: the peak intensity of the line,  $T_{\text{peak}}$  (in K); the intensity-weighted mean velocity of the line,  $v_{\text{mean}}$  (in  $\text{km s}^{-1}$ ); the full width at half maximum of the line,  $v_{\text{FWHM}}$  (in  $\text{km s}^{-1}$ ); and the integrated intensity of the line,  $I_{\text{CO}}$  (in  $\text{K km s}^{-1}$ ). Because the FCRAO

survey data are not electronically available, we use the values of these parameters reported by Young et al. (1995).

#### 5.4.1. CO Velocity and Line Width

The line width and mean velocity are not expected to vary strongly between the CO  $J = 2 \rightarrow 1$  and  $J = 1 \rightarrow 0$  transition. Therefore comparing our measurements of these quantities to those from earlier surveys allows a basic check on our data. Overall, this exercise confirms that we measure the same basic line shapes found by previous surveys at matched positions and resolution. We show this in the top two panels of Figure 34 and

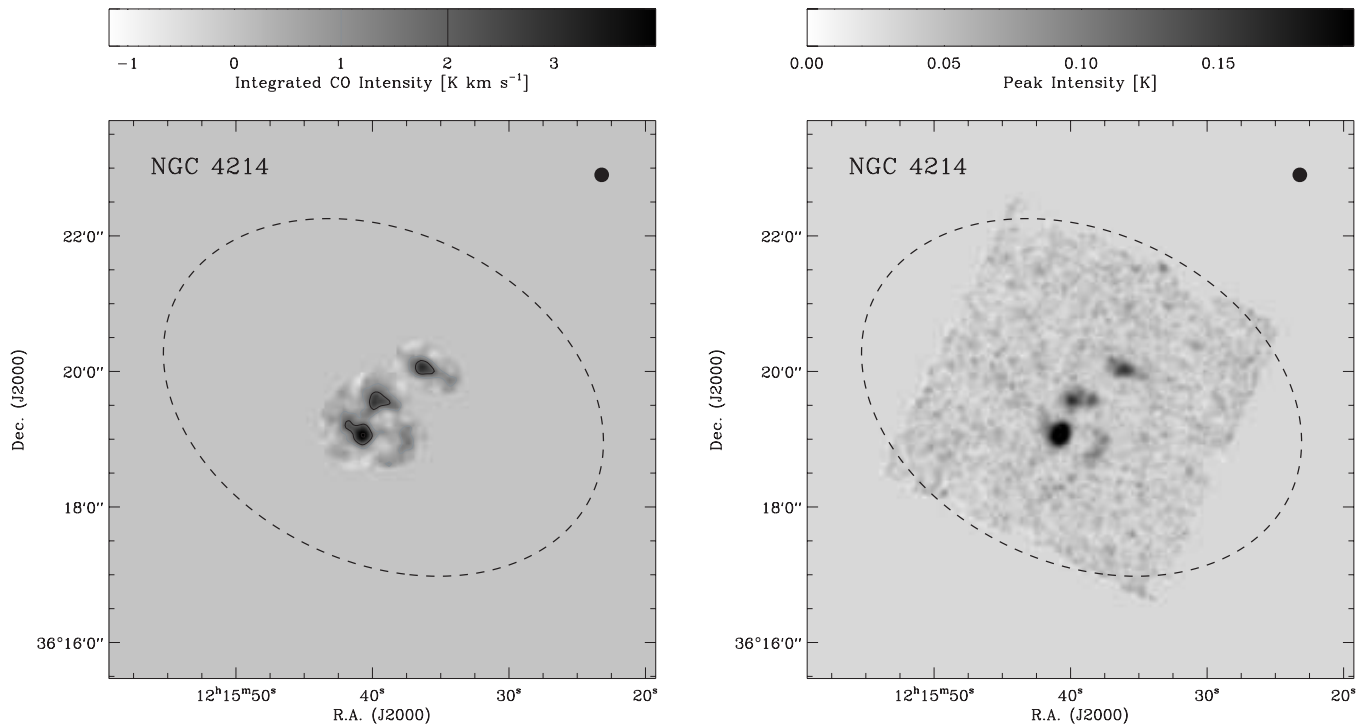


Figure 26. As Figure 17 but for NGC 4214.

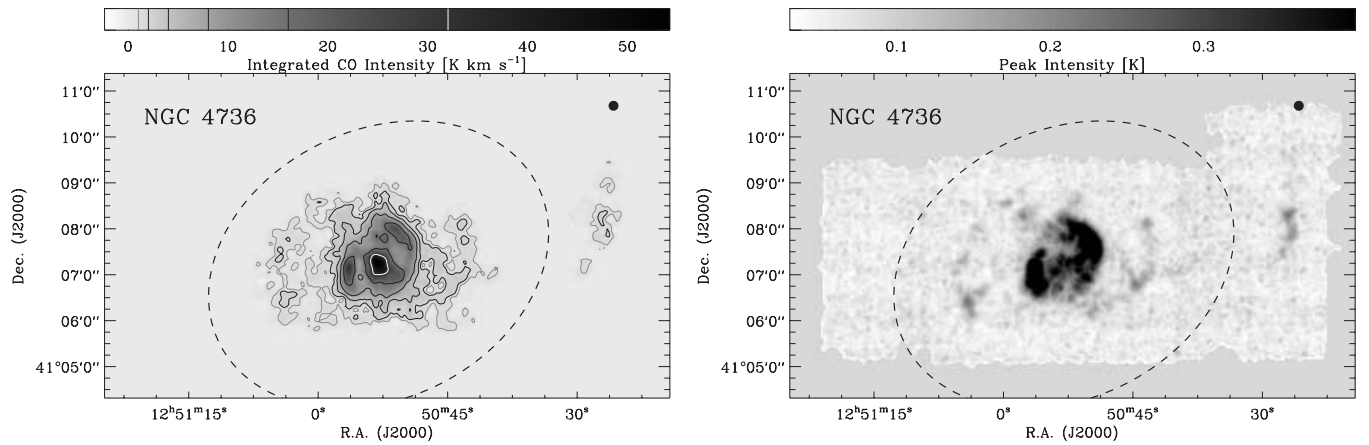


Figure 27. As Figure 17 but for NGC 4736.

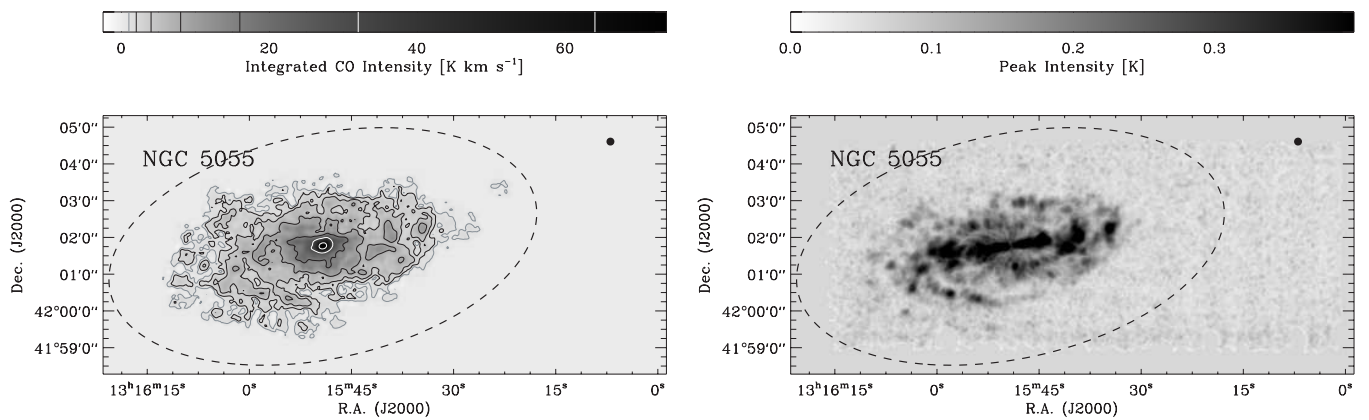


Figure 28. As Figure 17 but for NGC 5055.

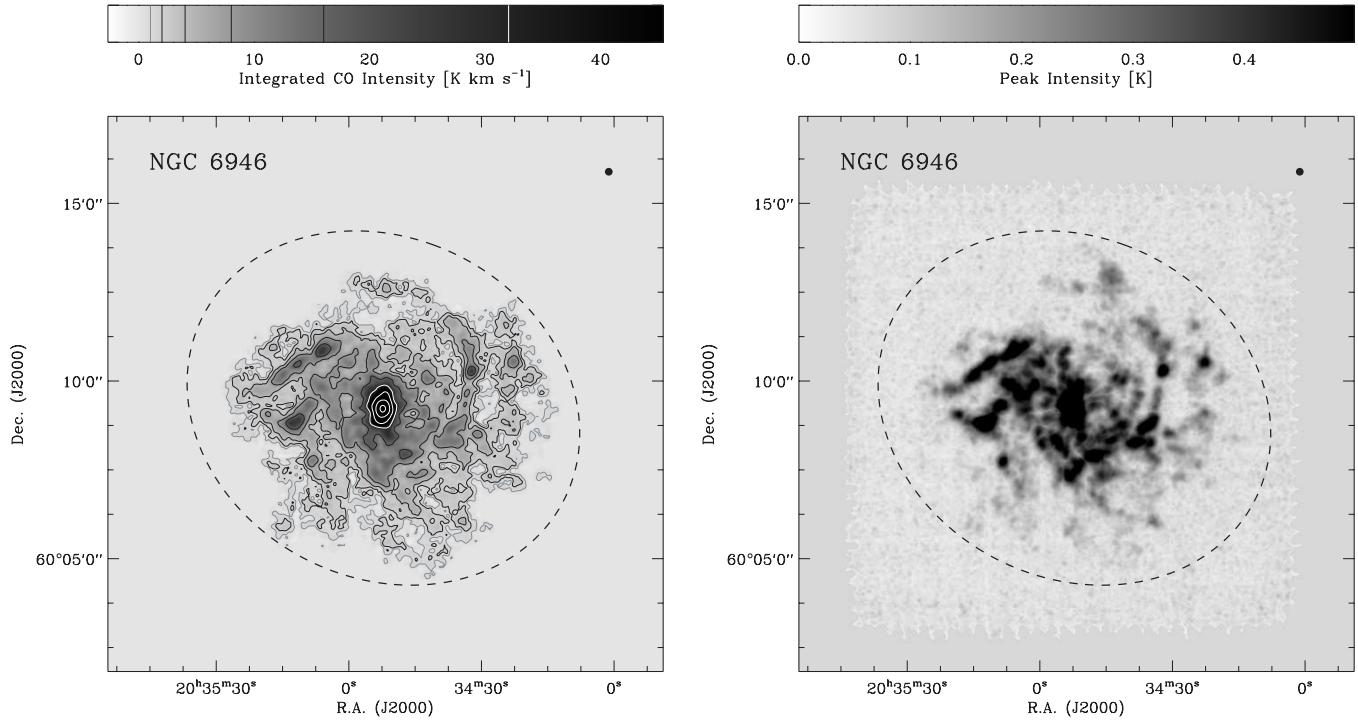


Figure 29. As Figure 17 but for NGC 6946.

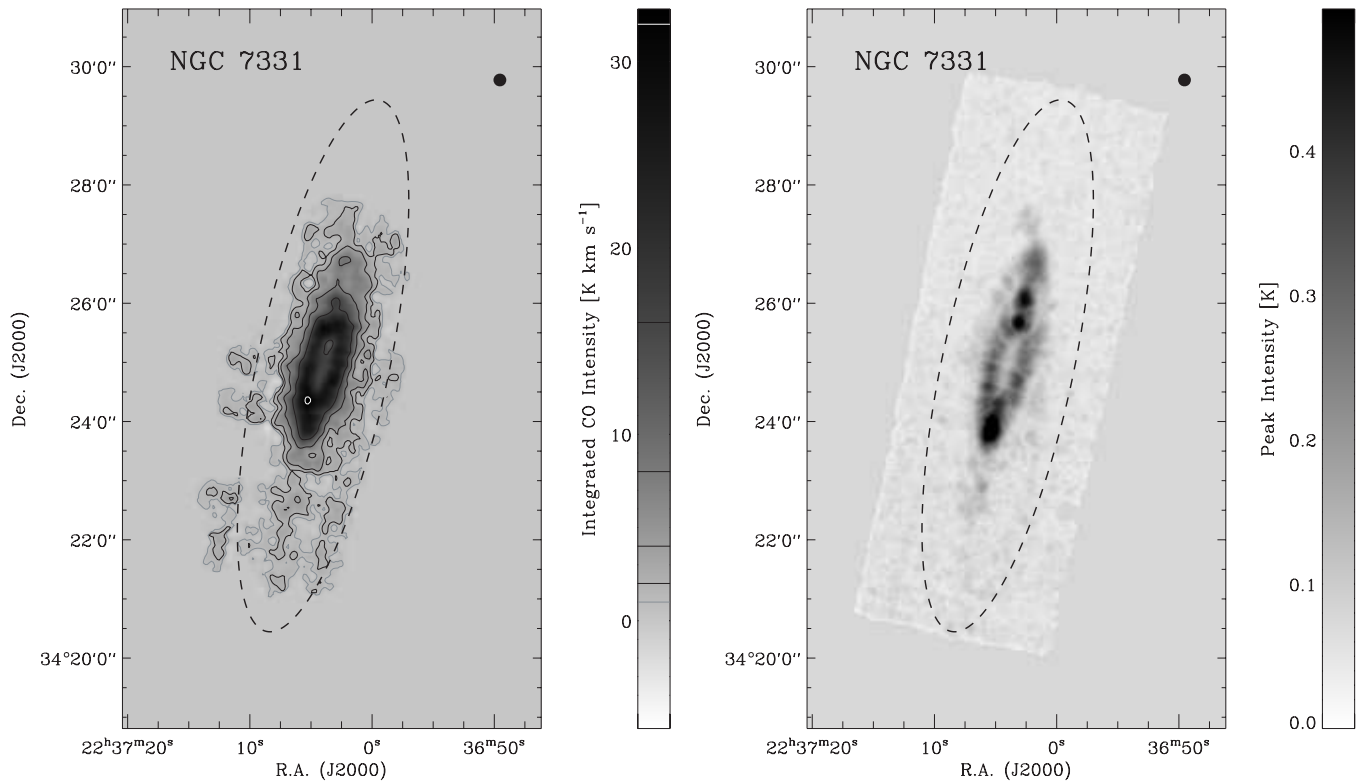


Figure 30. As Figure 17 but for NGC 7331.

the first two lines of Table 4, which give mean velocity offset and line width ratio (with equal weight to each galaxy).

The top left panel of Figure 34 shows the distribution of differences between the intensity-weighted mean CO  $J = 2 \rightarrow 1$  (HERACLES) velocity and the intensity-weighted mean CO  $J = 1 \rightarrow 0$  velocity. Each comparison survey appears as a separate, normalized histogram. A thick dashed line shows a

Gaussian fit to the average of the BIMA SONG, NRAO 12 m, and Kuno et al. (2007) histograms. This Gaussian is centered at  $-1.2 \text{ km s}^{-1}$  and has  $1\sigma$  width  $5.6 \text{ km s}^{-1}$ , identical with the uncertainties to what we found comparing CO  $J = 2 \rightarrow 1$  to H I.

The top right panel of Figure 34 shows the FWHM line width,  $v_{\text{FWHM}}$ , from HERACLES measured as a function of  $v_{\text{FWHM}}$

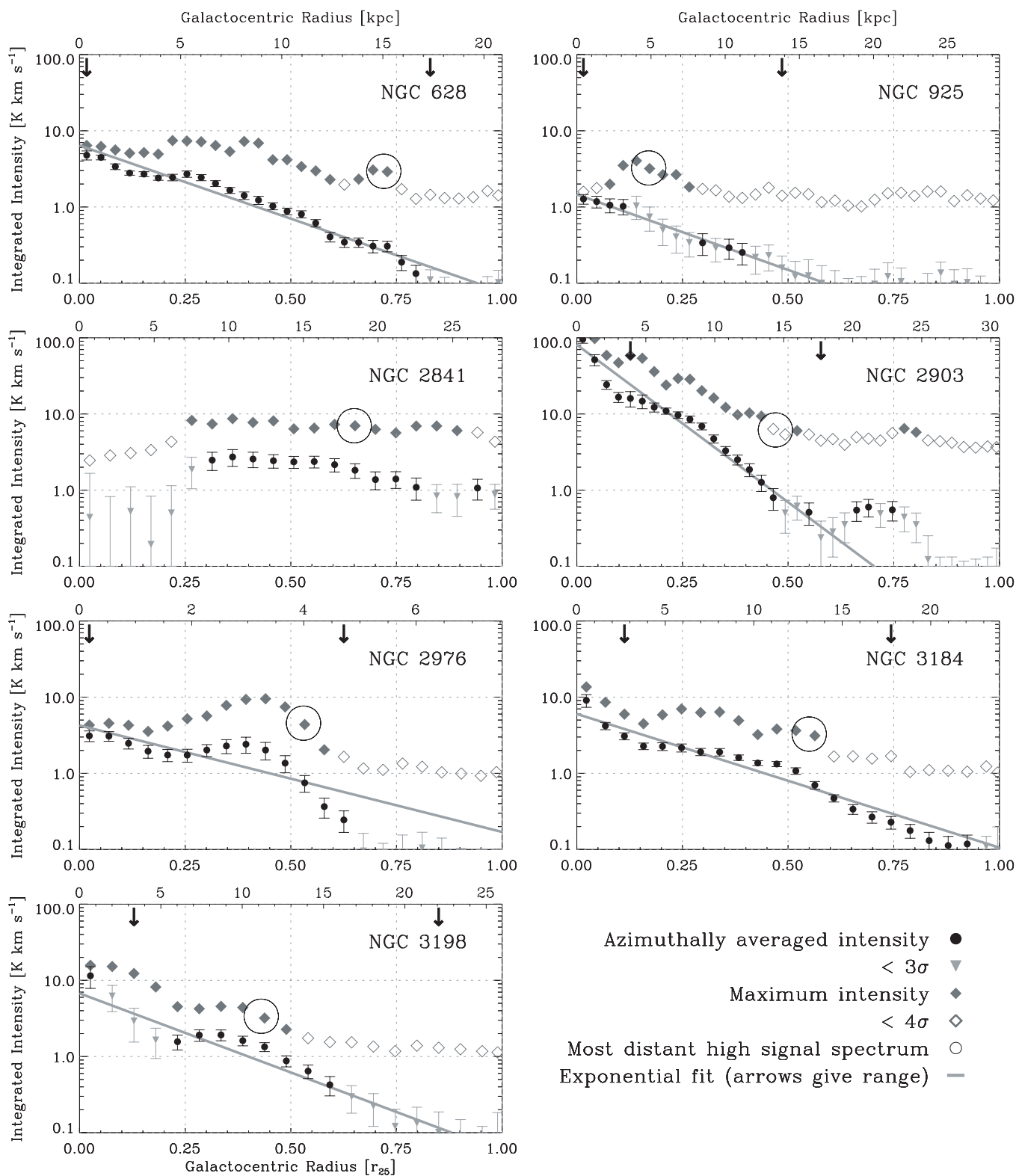


**Figure 31.** Integrated CO  $J = 2 \rightarrow 1$  intensity, in  $\text{K km s}^{-1}$ , as a function of galactocentric radius in units of  $r_{25}$  (bottom) and kpc (top). Black circles and gray triangles show the intensity averaged over  $10''$  wide tilted rings. Gray triangles indicate where the measurement divided by the rms uncertainty is  $< 3$ . Diamonds display the maximum intensity in each ring, with filled symbols showing where this value is clearly higher than expected from noise alone. The dark gray line shows the best-fit scale length. Arrows at the top of the plot bracket the region over which we carry out this fit. Large open circles indicate the location of the most distant high signal spectrum (Section 4.2).

from other surveys. Error bars show  $1\sigma$  uncertainty, estimated by repeatedly adding the measured noise to each spectrum and re-measuring  $v_{\text{FWHM}}$  (without the FCRAO spectra, we cannot

estimate uncertainties for these data). As with the mean velocity, there is general good agreement between HERACLES, BIMA SONG, the NRAO 12 m, and Kuno et al. (2007). There are



**Table 4**  
Comparison of HERACLES and Other Surveys

Quantity	FCRAO Survey	NRAO 12 m	BIMA SONG	Kuno et al. (2007)
$\Delta v_{\text{mean}}$ (km s <sup>-1</sup> ) <sup>a</sup>	-2.9	3.6	2.4	-0.4
ratio of $v_{\text{FWHM}}$ <sup>a</sup>	1.01	1.05	1.18	0.93
ratio of $T_{\text{peak}}$ <sup>a</sup>	0.76	0.87	0.67	0.81
ratio of $I_{\text{CO}}$ <sup>a</sup>	0.71	0.87	0.84	0.74

**Note.** <sup>a</sup> Values are mean difference (HERACLES—other survey) or ratio (HERACLES/other survey) giving equal weight to each galaxy.

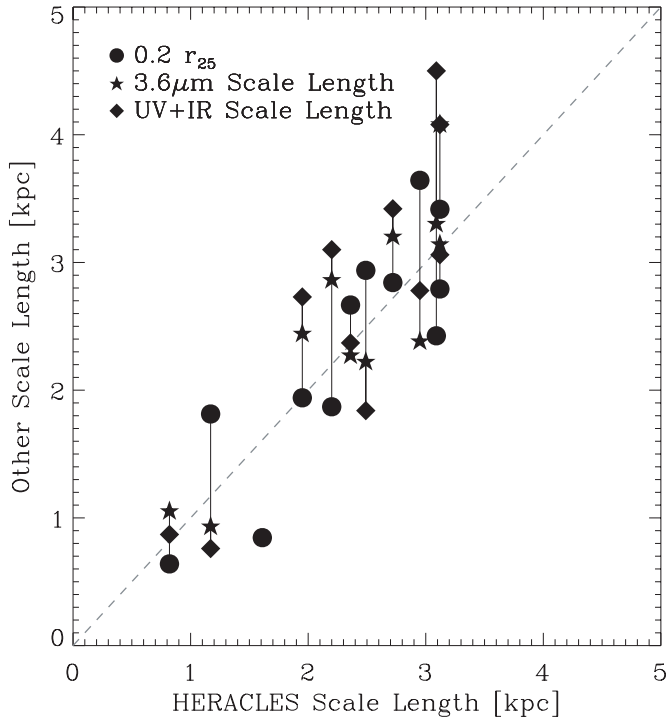


**Figure 32.** Several sizes for our targets (y-axis) as a function of the exponential scale lengths fit to the azimuthally average profiles (x-axis). Circles show  $0.2r_{25}$ ; stars show the  $3.6\ \mu\text{m}$  scale length, a tracer of the old stellar distribution; and diamonds show the scale length *GALEX*FUV + *Spitzer*  $24\ \mu\text{m}$  emission. Vertical lines connect points from the same galaxy. The dashed line shows equality.

with the FCRAO survey. We note that (1) the FCRAO survey is the only data set from which we do not ourselves measure the line parameters, so methodology may drive some of the difference; (2) these are the only data which are not maps, so it is not easy to tell whether pointing offsets may affect the comparison.

#### 5.4.2. CO $J = 2 \rightarrow 1/J = 1 \rightarrow 0$ Line Ratio

The ratio of CO  $J = 2 \rightarrow 1$  measured by HERACLES to CO  $J = 1 \rightarrow 0$  emission measured by previous surveys reflects both the relative calibrations of the telescopes and the line ratio,  $R_{21} = I_2 \rightarrow 1 / I_1 \rightarrow 0$ , which depends on the optical depth and excitation temperature of the gas. Generally speaking,  $R_{21} > 1$  indicates warm, optically thin gas. Optically thick gas produces  $R_{21} \approx 0.5\text{--}1.0$  with the value reflecting the temperature of the gas, though in low-density regions the levels may not be populated according to local thermodynamic equilibrium (LTE; see, e.g., Eckart et al. 1990, for a more thorough discussion).

In the bottom left panel of Figure 34, we plot the peak temperatures measured by HERACLES (y-axis) as a function of the peak temperature measured from other surveys at matched

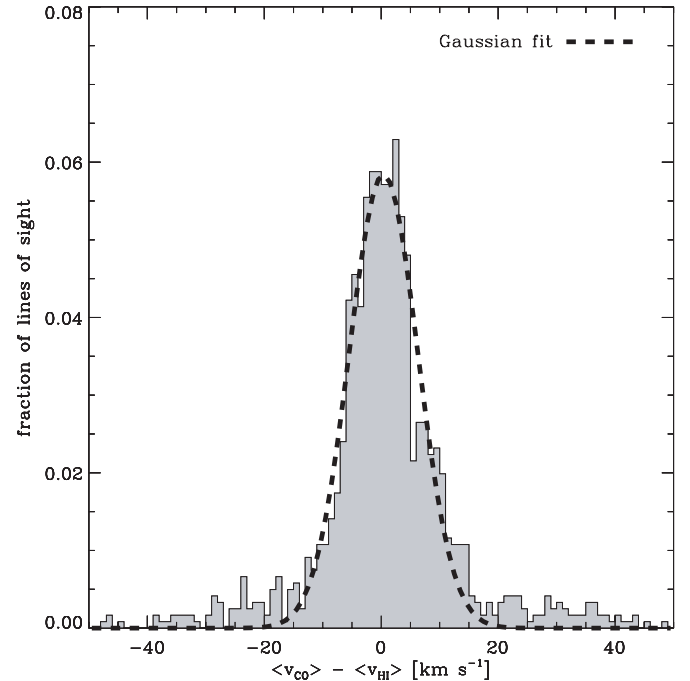


**Figure 33.** Distribution of  $\langle v_{\text{CO}} \rangle - \langle v_{\text{HI}} \rangle$ , the difference between the intensity-weighted mean CO velocity (from HERACLES) and intensity-weighted mean H I velocity (from THINGS), along lines of sight with good signal-to-noise. The best-fit Gaussian (dashed line) has  $1\sigma$  width  $5.9\ \text{km s}^{-1}$  and center  $-0.1\ \text{km s}^{-1}$ .

position and resolution (x-axis). We use the peak temperature because it avoids any concern related to the line profile or range of integration. We do not plot error bars, but recall that our condition to include a spectrum in this analysis was that  $T_{\text{peak}}$  have  $\text{SNR} > 5$  (meaning the statistical uncertainty on the ratio is always  $1\sigma < 30\%$ ). Table 5 compiles the average peak temperature ratio for each galaxy and survey and notes several measurements from the literature.

The ratios in Table 5 span 0.48–1.06, with most values between 0.6 and 1.0. These values agree with previous observations of the Milky Way and other galaxies. CO emission in the Milky Way comes mostly from optically thick regions and typical line ratios are  $\sim 0.6\text{--}0.8$  in the disk and  $\sim 1$  toward the Galactic center (Sakamoto et al. 1995; Oka et al. 1996, 1998). In the central regions of other galaxies, Braine & Combes (1992) found an average line ratio  $\sim 0.9$ . Casoli et al. (1991) compile observations on a number of galaxies and report typical values of  $\sim 1$  in galaxy nuclei and  $0.5\text{--}0.7$  in galaxy disks.

If the gas is optically thick, a ratio of 0.6 corresponds to an excitation temperature of  $\sim 5\ \text{K}$ , 0.8 to  $\sim 10\ \text{K}$ , and 0.9 to  $\sim 21\ \text{K}$ . Higher excitation temperatures yield a line ratio  $\sim 1$ . The average of all the values in Table 5 is 0.81, which is consistent with optically thick gas with an excitation temperature  $\sim 10\ \text{K}$ . One

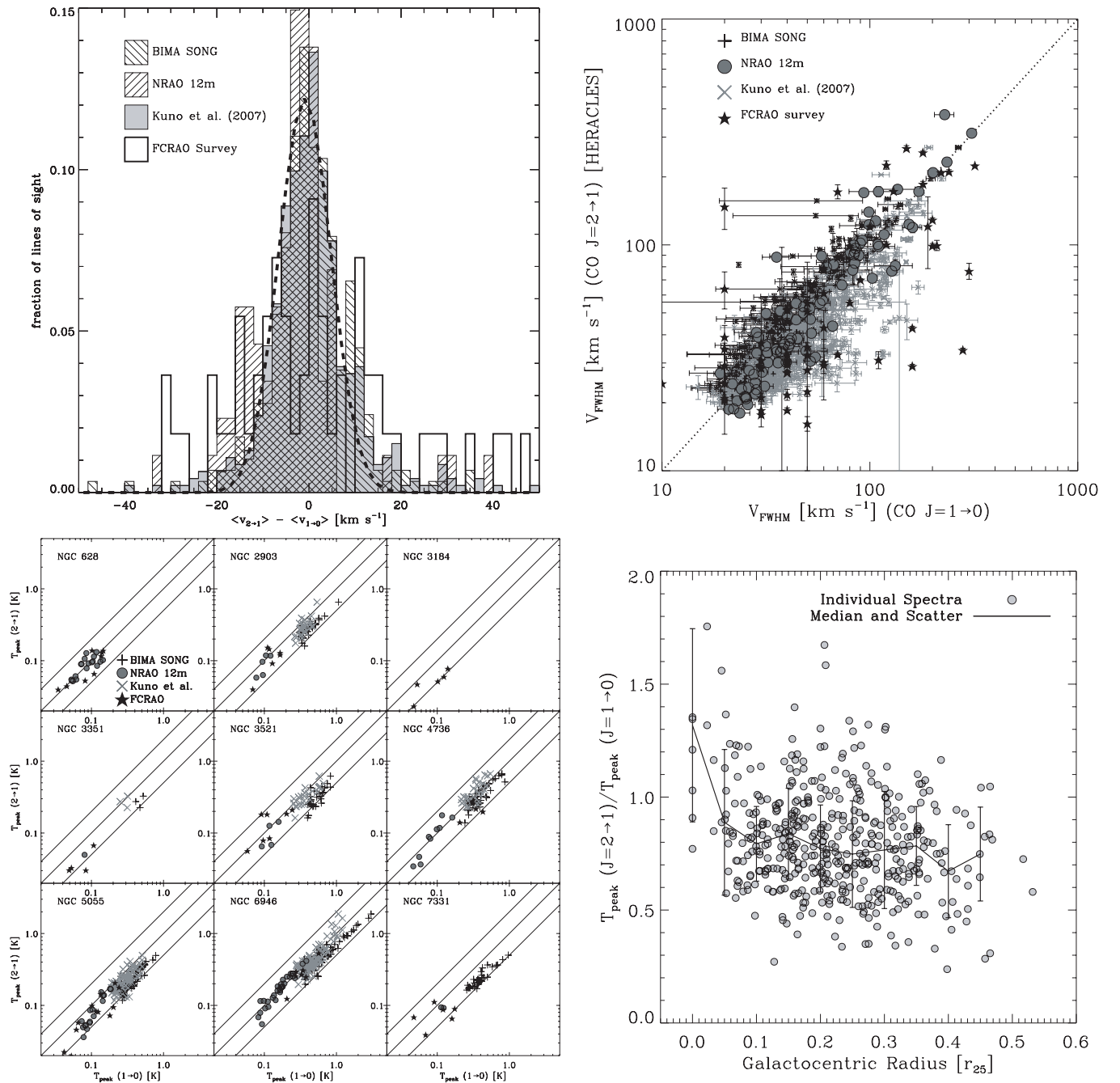


**Figure 34.** Comparison of HERACLES to previous CO  $J = 1 \rightarrow 0$  surveys. Top left: normalized histograms show the difference between intensity weighted mean velocity measured by HERACLES and four surveys of CO  $1 \rightarrow 0$  emission. A thick dashed line shows a Gaussian fit to the average of the BIMA SONG, the NRAO 12 m, and Kuno et al. (2007) histograms (center  $-1.2$  km s<sup>-1</sup>,  $1\sigma$  width  $5.6$  km s<sup>-1</sup>). Top right: the full line width at half maximum ( $v_{\text{FWHM}}$ ) measured by HERACLES (y-axis) as a function of  $v_{\text{FWHM}}$  measured the same CO  $J = 1 \rightarrow 0$  surveys. The dotted line shows equality. Bottom left: peak temperature (intensity) in the HERACLES CO  $J = 2 \rightarrow 1$  spectrum as a function of peak temperature in the CO  $J = 1 \rightarrow 0$  spectrum at the same position and resolution. From top to bottom, solid lines show ratios of 2.0, 1.0, and 0.5. Bottom right: ratio of peak CO  $J = 2 \rightarrow 1$  temperature (intensity) measured by HERACLES to peak CO  $J = 1 \rightarrow 0$  temperature measured Kuno et al. (2007) as a function of galactocentric radius normalized to  $r_{25}$ . Each gray point indicates an individual pair of high significance spectra. The black points and lines show the median and scatter for the data in bins  $0.05r_{25}$  wide with the first bin centered at 0.

should treat this temperature with caution: we do not constrain the optical depth (e.g., using one of the isotopes of CO) and we have no verification that our sources are in LTE, so subthermally excited, low-density envelopes—which are observed in Galactic GMCs—may lower the overall intensity ratio (e.g., Sakamoto et al. 1994).

There is noticeable scatter among the peak temperature ratios derived from different data sets for the same galaxy. Some scatter may arise from differences in resolutions or area considered

(the set of spectra with peak SNR  $> 5$  varies with comparison survey). If we ignore these explanations, Table 5 suggests that there are systematic calibration differences among the various surveys at the  $\sim 10\%$  level and that the calibration of a given galaxy in a given survey is uncertain by  $\sim 15\%$ . These uncertainties seem reasonable for millimeter line observations and agree with the scatter in comparisons with the FCRAO survey carried out by Helfer et al. (2003, their Figure 51) and Kuno et al. (2007, their Figure 1).

**Table 5**  
Average  $T_{\text{peak}}$  Ratio by Galaxy and Survey<sup>a</sup>

Galaxy	FCRAO Survey	NRAO 12 m	BIMA SONG	Kuno et al. (2007)	Other <sup>b</sup>
NGC 628	0.93	1.01	...	...	0.44
NGC 2841	0.72	...	...	...	
NGC 2903	0.91	0.90	0.68	0.82	0.6–0.9
NGC 3184	0.59	...	...	0.60	
NGC 3351	0.50	0.62	0.59	0.95	1.65
NGC 3521	1.14	0.81	0.59	0.86	
NGC 4736	0.70	1.02	0.83	1.12	
NGC 5055	0.71	0.77	0.64	0.79	
NGC 6946	0.85	1.03	0.77	0.92	0.8
NGC 7331	0.82	0.79	0.60	...	0.5

**Notes.**

<sup>a</sup> Mean ratio of peak CO  $J = 2 \rightarrow 1$  temperature to peak CO  $J = 1 \rightarrow 0$  temperature.

<sup>b</sup> Integrated intensity (*not* peak temperature) ratios drawn from the literature. References: NGC 628, NGC 3351, NGC 7331–Braine et al. (1993); NGC 2903–Jackson et al. (1991); NGC 6946–Crosthwaite & Turner (2007)

Because  $R_{21}$  is observed to vary between the center and the disk in both the Milky Way and other galaxies, the bottom right panel of Figure 34 shows the ratio of  $T_{\text{peak}}$  in the two transitions as a function of galactocentric radius. This plot shows only data from HERACLES and Kuno et al. (2007). These data most closely match our own in observing strategy, instrumentation, and resolution, making them the best option for this comparison. Black points connected by lines show the median ratio in bins  $0.05r_{25}$  with the first bin centered at 0. In the centers of galaxies, we observe the same trend noted by Casoli et al. (1991) and found in the Milky Way: the ratio is high ( $\sim 1.3$ ) in the center of the galaxy and then drops rapidly to  $\sim 0.8$ , remaining almost constant at this value out to the edge of our comparison at  $\sim 0.45r_{25}$ . This constancy must be interpreted with care. By selecting only high significance spectra, we bias ourselves to bright regions. This may have the effect of creating a homogeneous data set while omitting lower intensity emission that accounts for a significant fraction of the emission at large radii.

## 6. SUMMARY

This paper presents the HERA CO Line Extragalactic Survey (HERACLES), a new survey of CO  $J = 2 \rightarrow 1$  emission from nearby galaxies obtained using the IRAM 30 m. Because on-the-fly mapping mode with the multipixel HERA allows us to efficiently map large areas with good sensitivity and adequate resolution, HERACLES targets a wider area than previous surveys. Most maps extend to the edge of the optical disk, defined by the isophotal radius  $r_{25}$ .

Our sample overlaps THINGS and SINGS, allowing easy comparison to data from radio to UV wavelengths. One application of this multiwavelength data allows us to automate our reduction. We use the mean H I velocity from THINGS as a prior to define baseline fitting regions and are thus able to reduce  $10^7$  spectra in a robust, automated manner. We verify the assumption that CO and H I exhibit the same mean velocity by direct comparison of HERACLES and THINGS mean velocities, finding little or no systematic difference. We also confirm that our automated approach matches a by-hand reduction well.

We clearly detect 14 galaxies and place upper limits on CO  $2 \rightarrow 1$  emission from 4 low metallicity, irregular dwarf galaxies. For a Galactic CO-to- $H_2$  conversion factor, the implied  $H_2$

masses are mostly 0.2–0.6 times the H I mass and 0.03–0.1 times the stellar mass. More detailed analysis of the relationship between  $H_2$ , H I, stars, and star formation in our sample is presented elsewhere (Bigiel et al. 2008; Leroy et al. 2008).

We illustrate the distribution of CO in the detected galaxies via channel maps, azimuthally averaged profiles, and intensity maps. Where we find emission, the brightness is usually consistent with  $\sim 5\%$ – $15\%$  of the area inside the beam being covered by Galactic GMCs, though in a few regions the implied surface density averaged over our  $\sim 500$  pc beam exceeds that of a Galactic GMC. The line width and mean velocity that we derive agree reasonably with previous (CO  $J = 1 \rightarrow 0$ ) surveys; systematic differences among surveys do exist, with magnitude  $\sim 10\%$ – $20\%$ , but HERACLES never appears to be an outlier.

The ratio of CO  $J = 2 \rightarrow 1$  intensity to CO  $J = 1 \rightarrow 0$  intensity for high significance spectra lies mostly in the range 0.6–1.0 with an average value of 0.8, comparable to that found in the inner Milky Way. This could be produced by optically thick gas with an excitation temperature  $\sim 10$  K, though this temperature should not be over-interpreted without constraints on the optical depth or applicability of LTE. This line ratio is higher ( $\sim 1.3$ ) in the centers of galaxies and then roughly constant as a function of radius, though we caution that strong selection effects may be at work.

Our detections include high significance emission from the outer part of the star-forming disk in several galaxies. We also find bright CO emission associated with an H I filament outside the main disk of NGC 4736 (radius  $1.33r_{25}$ ). The azimuthally averaged intensity usually declines smoothly even beyond these detections and we are sensitive to only the most massive individual GMCs. Therefore we would expect to find many more such regions with improved sensitivity.

Although the channel and integrated intensity maps show a variety of morphologies, the azimuthally averaged profiles are well described by exponential declines. The best-fit scale lengths range from 0.8–3.2 kpc and correlate closely with optical radius, near-IR (stellar mass) scale length, and UV+IR (star formation) scale length. These results are in good agreement with previous findings that CO emission closely follows both the stellar light and distribution of star formation on large scales. The exponential decline in CO brightness is a combination of decreasing maximum brightness of CO emission and a decreased filling fraction of bright CO emission at large radii.

We thank the anonymous referee for helpful comments. We thank Jérôme Pety for his help with the CLASS portion of the reduction pipeline, and the IRAM 30-m staff for their help with the observations, in particular operators Juan Luis Santarén, Frédéric Damour, Enrique Lobato, and Mariano Espinosa and support astronomers Gabriel Paubert, Rebeca Aladro, and Denise Riquelme. FB acknowledges support from the Deutsche Forschungsgemeinschaft (DFG) Priority Program 1177. AU has been supported through a Post Doctoral Research Assistantship from the UK Science & Technology Facilities Council. The work of WJGdB is based upon research supported by the South African Research Chairs Initiative of the Department of Science and Technology and National Research Foundation. We acknowledge use of the NASA/IPAC Extragalactic Database (NED) which is operated by the Jet Propulsion Laboratory, California Institute of Technology, under contract with the National Aeronautics and Space Administration; the HyperLeda catalog, located on the World Wide Web at <http://www-obs.univ-lyon1.fr/hypercat/intro.html>; and NASA's Astrophysics Data System (ADS).

## REFERENCES

- Bigiel, F., Leroy, A., Walter, F., Brinks, E., de Blok, W. J. G., Madore, B., & Thornley, M. D. 2008, *AJ*, **136**, 2846
- Blitz, L. 1993, in *Protostars and Planets III*, ed. E. H. Levy & J. I. Lunine (Tucson, AZ: Univ. of Arizona Press), 125
- Braine, J., & Combes, F. 1992, *A&A*, **264**, 433
- Braine, J., Combes, F., Casoli, F., Dupraz, C., Gerin, M., Klein, U., Wielebinski, R., & Brouillet, N. 1993, *A&AS*, **97**, 887
- Braine, J., Ferguson, A. M. N., Bertoldi, F., & Wilson, C. D. 2007, *ApJ*, **669**, L73
- Casoli, F., Dupraz, C., Combes, F., & Kazès, I. 1991, *A&A*, **251**, 1
- Crosthwaite, L. P., & Turner, J. L. 2007, *AJ*, **134**, 1827
- Dame, T. M., Hartmann, D., & Thaddeus, P. 2001, *ApJ*, **547**, 792
- de Blok, W. J. G., Walter, F., Brinks, E., Trachternach, C., Oh, S.-H., & Kennicutt, R. C. 2008, *AJ*, **136**, 2648
- Désert, F. X., Bazell, D., & Boulanger, F. 1988, *ApJ*, **334**, 815
- Eckart, A., Downes, D., Genzel, R., Harris, A. I., Jaffe, D. T., & Wild, W. 1990, *ApJ*, **348**, 434
- Engargiola, G., Plambeck, R. L., Rosolowsky, E., & Blitz, L. 2003, *ApJS*, **149**, 343
- Fukui, Y., et al. 1999, *PASJ*, **51**, 745
- Helfer, T. T., Thornley, M. D., Regan, M. W., Wong, T., Sheth, K., Vogel, S. N., Blitz, L., & Bock, D. C.-J. 2003, *ApJS*, **145**, 259
- Israel, F. P., et al. 1984, *A&A*, **134**, 396
- Jackson, J. M., Eckart, A., Cameron, M., Wild, W., Ho, P. T. P., Pogge, R. W., & Harris, A. I. 1991, *ApJ*, **375**, 105
- Kennicutt, R. C., Jr., et al. 2003, *PASP*, **115**, 928
- Kuno, N., et al. 2007, *PASJ*, **59**, 117
- Lebrun, F., et al. 1983, *ApJ*, **274**, 231
- Leroy, A., Bolatto, A., Walter, F., & Blitz, L. 2006, *ApJ*, **643**, 825
- Leroy, A. K., Walter, F., Brinks, E., Bigiel, F., de Blok, W. J. G., Madore, B., & Thornley, M. D. 2008, *AJ*, **136**, 2782
- Mangum, J. G., Emerson, D. T., & Greisen, E. W. 2007, *A&A*, **474**, 679
- Oka, T., Hasegawa, T., Handa, T., Hayashi, M., & Sakamoto, S. 1996, *ApJ*, **460**, 334
- Oka, T., Hasegawa, T., Hayashi, M., Handa, T., & Sakamoto, S. 1998, *ApJ*, **493**, 730
- Regan, M. W., Thornley, M. D., Helfer, T. T., Sheth, K., Wong, T., Vogel, S. N., Blitz, L., & Bock, D. C.-J. 2001, *ApJ*, **561**, 218
- Rickard, L. J., Palmer, P., Morris, M., Turner, B. E., & Zuckerman, B. 1975, *ApJ*, **199**, L75
- Rosolowsky, E. 2007, *ApJ*, **654**, 240
- Sakamoto, K., Okumura, S. K., Ishizuki, S., & Scoville, N. Z. 1999, *ApJS*, **124**, 403
- Sakamoto, S., Hasegawa, T., Hayashi, M., Handa, T., & Oka, T. 1995, *ApJS*, **100**, 125
- Sakamoto, S., Hayashi, M., Hasegawa, T., Handa, T., & Oka, T. 1994, *ApJ*, **425**, 641
- Schuster, K.-F., et al. 2004, *A&A*, **423**, 1171
- Schuster, K. F., Kramer, C., Hitschfeld, M., García-Burillo, S., & Mookerjee, B. 2007, *A&A*, **461**, 143
- Solomon, P. M., & de Zafra, R. 1975, *ApJ*, **199**, L79
- Solomon, P. M., Rivolo, A. R., Barrett, J., & Yahil, A. 1987, *ApJ*, **319**, 730
- Strong, A. W., & Mattox, J. R. 1996, *A&A*, **308**, L21
- Strong, A. W., et al. 1988, *A&A*, **207**, 1
- Walter, F., Brinks, E., de Blok, W. J. G., Bigiel, F., Kennicutt, R. C., Thornley, M. D., & Leroy, A. 2008, *AJ*, **136**, 2563
- Walter, F., Taylor, C. L., Hüttemeister, S., Scoville, N., & McIntyre, V. 2001, *AJ*, **121**, 727
- Wilson, B. A., Dame, T. M., Masheded, M. R. W., & Thaddeus, P. 2005, *A&A*, **430**, 523
- Wilson, R. W., Jefferts, K. B., & Penzias, A. A. 1970, *ApJ*, **161**, L43
- Young, J. S., & Scoville, N. Z. 1991, *ARA&A*, **29**, 581
- Young, J. S., et al. 1995, *ApJS*, **98**, 219